

High resolution observations of sulphide alteration textures

Bachelor Thesis

Freie Universität Berlin

Author: Jasper Engelmann

Supervisor: Prof. Dr. Esther Schwarzenbach

Second Supervisor: Dr. Johannes C. Vrijmoed

Submitted: 24.08.2020

Eigenständigkeitserklärung

Hiermit erkläre ich, dass ich die vorliegende Arbeit selbstständig verfasst und keine anderen als die angegebenen Quellen und Hilfsmittel benutzt habe.

Alle sinngemäß und wörtlich übernommenen Textstellen aus fremden Quellen wurden kenntlich gemacht.

Berlin, den 22.08.2020

Jasper Engelmann

Declaration of originality

I confirm that the submitted thesis is original work and was written by me without further assistance. Appropriate credit has been given where reference has been made to the work of others.

Berlin, 22.08.2020

Jasper Engelmann

Abstract

The usually small sulphide phase in serpentinized peridotites is of interest when trying to evaluate reaction conditions during alteration, such as f_{O_2} , a_{H_2} and $a_{H_{2S}}$, with one important indication being the occurrence of native metals and metal alloys. Using high resolution imaging and element mapping on samples from an active, continental serpentinization area in southwestern Turkey, sulphides, their composition and mineralogy, elemental distribution, and textures on a scale down to 30nm are described in this thesis. At least two stages of fluid-rock-interaction are visible in the samples. With phase relations in the Fe-Ni-O-S and Fe-Ni-Co-S systems, precipitation temperatures for the sulphides (200-300°C) and activities of H₂ ($>10^{-2}$) and H_{2S} ($<10^{-4}$) during later, ongoing lower-temperature (50-100°C) alteration of the grains are estimated. In the microtextures, which display a fibre-like intergrowth of awaruite and silicate in reaction zones within pentlandite, part of the process which replaces pentlandite with awaruite can be observed. Some sulphides are enriched in Cu, possibly indicating another, Cu-bearing fluid interacting with the rocks.

Table of Contents

Introduction.....	1
Oceanic lithosphere and serpentinization	1
Obduction and ophiolites.....	2
Sulphides in serpentinite.....	2
Goal of this thesis	3
Geological setting	3
Methods	5
Polarization microscopy	5
Scanning electron microscopy.....	5
The scanning electron microscope.....	5
Sample preparation and measurements.....	6
Electron microprobe.....	7
Results	8
General sample composition.....	8
Overall sulphide content.....	8
Observations in the grains.....	10
1. Pentlandite with a μm -scale rim of awaruite	10
2. Pentlandite with reaction zones that are part fibre-like , part awaruite	11
3. Pentlandite with magnetite and sometimes elevated Cu-contents.....	14
4. Lightly broken up pentlandite	17
Discussion.....	17
Sulphide micro- and nanotextures	17
Primary and secondary minerals.....	18
Using the composition of sulphides to estimate alteration conditions	18
Interpreting the fibre-like texture in the grains of group 2.....	19
Conclusion	20
Publication bibliography.....	21
Appendix.....	24

Introduction

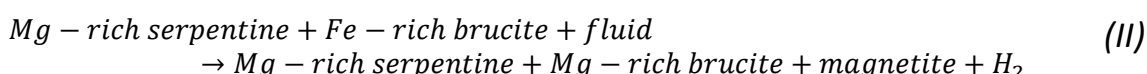
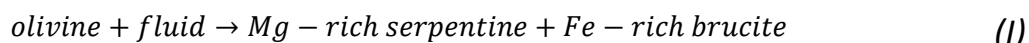
Oceanic lithosphere and serpentinization

Oceanic lithosphere is made up of the oceanic crust and some of the underlying mantle, with the typical ophiolite sequence summarised here by *Dilek and Furnes* (2014) from *Anonymous* (1972):

According to the definition proposed during the 1972 Penrose Conference, an ophiolite sequence consists, from bottom to top, of upper mantle peridotites, layered ultramafic–mafic rocks, layered to isotropic gabbros, sheeted dikes, extrusive rocks, and a sedimentary cover.

Ophiolite sequences are formed at mid ocean ridges by seafloor-spreading and the rate of spreading defines the exact sequence, with the full Penrose-type only occurring at fast spreading ridges. At slow-to ultra-slow spreading ridges, low melt supply requires tectonic extension of the seafloor and subsequent detachment faults with exposure of the underlying ultramafic rocks to accommodate for plate separation. This produces areas of the oceanic lithosphere that lack the usually mafic volcanic section (e.g. Bach and Früh-Green 2010). The exposed upper mantle peridotites are then often subject to hydrothermal alteration by oceanwater and heat provided by the underlying mantle or residual heat from the formation process, with faults and fractures from the tectonic activity as flow channels for the fluid. The hydrothermal alteration of a peridotite is known as serpentinization, the resulting rocks are called serpentinites.

Serpentinization takes place in several steps with different reactions, reaction conditions and compositions of fluid and rock occurring along the way. A very important part of the process the oxidation of Fe^{2+} to Fe^{3+} , which is part of a set of reactions that turn olivine and water into serpentine, brucite, magnetite and hydrogen, creating a highly reducing environment (Bach et al. 2006; Schwarzenbach et al. 2014):

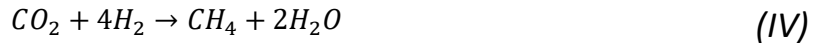


Brucite sometimes does not appear in the final mineral assemblage of a peridotite, despite being produced by serpentinization reactions. One way to explain this is through later dissolution of brucite as a sign of weathering on the ocean floor (Snow and Dick 1995), another explanation is a different reaction path, following *Andreani et al.* (2007):



The replacement of olivine with serpentine often produces a mesh-texture, with serpentine pseudomorphically replacing olivine (e.g. Bach and Früh-Green 2010). The reactions begin at the olivine grain boundaries and produce mesh-textured areas of serpentine replacing olivine, and magnetite appearing within the mesh-texture (e.g. Andreani et al. 2007). The mesh cores, formally the grain cores of olivine, remain as olivine at first, but complete serpentinization also turns them into serpentine. Serpentine can also pseudomorphically replace pyroxenes, the resulting texture is called a bastite.

Another effect of the hydrogen can be the reduction of CO₂, producing hydrocarbon gas, mostly methane (Berndt et al. 1996). The mechanisms that produce these hydrocarbons are Fischer Tropsch Type reactions, the name being derived from an industrial process to generate hydrocarbons from CO₂ and H₂. According to *Berndt et al.* (1996), this is the reaction that produces methane abiotically during serpentinization:



Additionally to methane, other hydrocarbons like ethane, propane, butane etc. are produced by Fischer Tropsch Type reactions in lower concentrations, decreasing with each C added to the chain (Berndt et al. 1996; Lollar et al. 2008).

Obduction and ophiolites

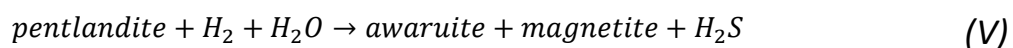
When an ocean closes, most of the oceanic plate is subducted underneath the upper plate, which can be either continental or also oceanic. An accretionary wedge, consisting of ‘scraped off’ sediment and lithosphere from the oceanic plate, can be obducted onto the upper plate rather than subducted (e.g. Dewey 1976). Obducted oceanic lithosphere is called an ophiolite. There are different types of ophiolites, depending on the setting in which the oceanic lithosphere formed and the mechanism that emplace the ophiolite onto the continental plate. Differentiating between formation mechanism is possible by analysing the ophiolite structure and observable sequence, most importantly the presence or absence of the mafic section, and the geochemistry of the resulting rocks. Different types include: Continental margin type, mid-ocean ridge types (MOR), Plume type, suprasubduction zone types (SSZ), and volcanic arc type (Dilek and Furnes 2014).

Sulphides in serpentinite

Peridotites commonly contain small amounts of primary sulphides as a residual phase from mantle melting. Elements often incorporated in the sulphide phase are Fe, Ni, Co, and Cu. In unaltered peridotites, common sulphides are (Co-)pentlandite, pyrrhotite and chalcopyrite (Lorand 1989a; Lorand 1989b). Stochiometric formulae for all minerals are presented in Table 1.

During serpentinization, the sulphide phase is often altered and reequilibrated, with the resulting sulphide mineral assemblage being highly dependent on the rate of alteration and fugacity or activity of oxygen, hydrogen, H₂S and other sulphur species (Eckstrand 1975; Klein and Bach 2009). In early stages of serpentinization, low-sulphur-assemblages are common and even native alloys and metals can occur (Abrajano and Pasteris 1989; Chamberlain et al. 1965; Lorand 1985; Nickel 1959; Schwarzenbach et al. 2014; Alt and Shanks 1998; Frost 1985). This indicates high hydrogen activity and low fugacities of oxygen and H₂S with widespread assemblages being pentlandite + awaruite + magnetite and pentlandite + heazlewoodite + magnetite (Klein and Bach 2009).

Together with very low oxygen and sulphur fugacities, the hydrogen produced by reaction (II) or (III) can desulphurize minerals like pentlandite, producing awaruite and magnetite and releasing H₂S (Klein and Bach 2009):



Once olivine is not available for serpentinization reactions [(I), (II), (III)] anymore, oxygen fugacity rises again and the native metals become unstable (Frost 1985), breaking down awaruite into magnetite and heazlewoodite (Klein and Bach 2009). This leads to higher sulphur contents in the opaque mineral

assemblages, with common minerals being, among others, pyrite and millerite (Klein and Bach 2009; Schwarzenbach et al. 2012).

Goal of this thesis

The goal of this thesis is to describe the micro- and nanotextures of sulphides in a serpentized peridotite and to infer their origin and formation mechanisms. A focus is on the occurrence, distribution and appearance of native metals and alloys, using chemical composition data and electron microscopy.

Geological setting

The samples analysed in this thesis come from the Chimaera seep, close to the town of Çıraklı in the Antalya Province, Turkey. The natural gas seep, also known as Yanartaş, meaning ‘flaming rock’ in Turkish, is part of the Tekirova ophiolitic unit. This unit belongs to the Antalya accretionary complex, which is one of the Neotethyan ophiolitic complexes in the eastern Mediterranean and an accretionary wedge obducted onto an autochthonous carbonate platform during the closing of the Neotethyan Ocean (Aldanmaz et al. 2009). The Neotethys formed by seafloor spreading in the middle to late Permian, and partial sub- and obduction are reported for the Cretaceous (e.g. Stampfli and Borel 2004 and sources therein). The thrust belt underlying the Tekirova unit has been dated to Cretaceous (90-94 Ma; Çelik et al. 2006) metamorphic ages.

The ophiolites in the Antalya Complex show evidence of more than one phase of oceanic crust formation, one being of the MOR type, a later one of SSZ type (Aldanmaz et al. 2009). It is likely that the samples discussed here are from an area that formed oceanic lithosphere through slow or ultraslow spreading, with tectonic extension leading to the exposure of peridotite to the ocean floor. This enabled serpentization, which probably occurred over a long period of time, presumably until either fluid, the reactants or sufficient thermal or chemical energy were not available anymore. During one of the above-mentioned ocean-closure related events, the block that is the Tekirova ophiolite today was obducted onto the upper plate.

Since the ophiolite has been obducted, it is no longer subject to ocean-water related alteration. It does, however, still host and circulate meteoric water (Meyer-Dombard et al. 2015), which leads to further alteration and ongoing continental serpentization to this day. The gas that is emitted from the seeps consists mainly of methane (~87 vol.%) and hydrogen (~10 vol.%), 80-90% of which are produced abiotically by serpentization and subsequent Fischer Tropsch Type reactions (Etiope et al. 2011). Estimated serpentization temperatures for the currently emitted gas by hydrogen isotopic composition are very low, around 50°C, but definitely below 100°C (Etiope et al. 2011). An ephemeral fluid seep on the site releases a fluid with a pH of 11.95, likely to be the product of ongoing serpentization (Meyer-Dombard et al. 2015).

The samples were collected from three outcrops, as described by *Etiope et al.* (2011), and shown in the map below (Fig. 1).

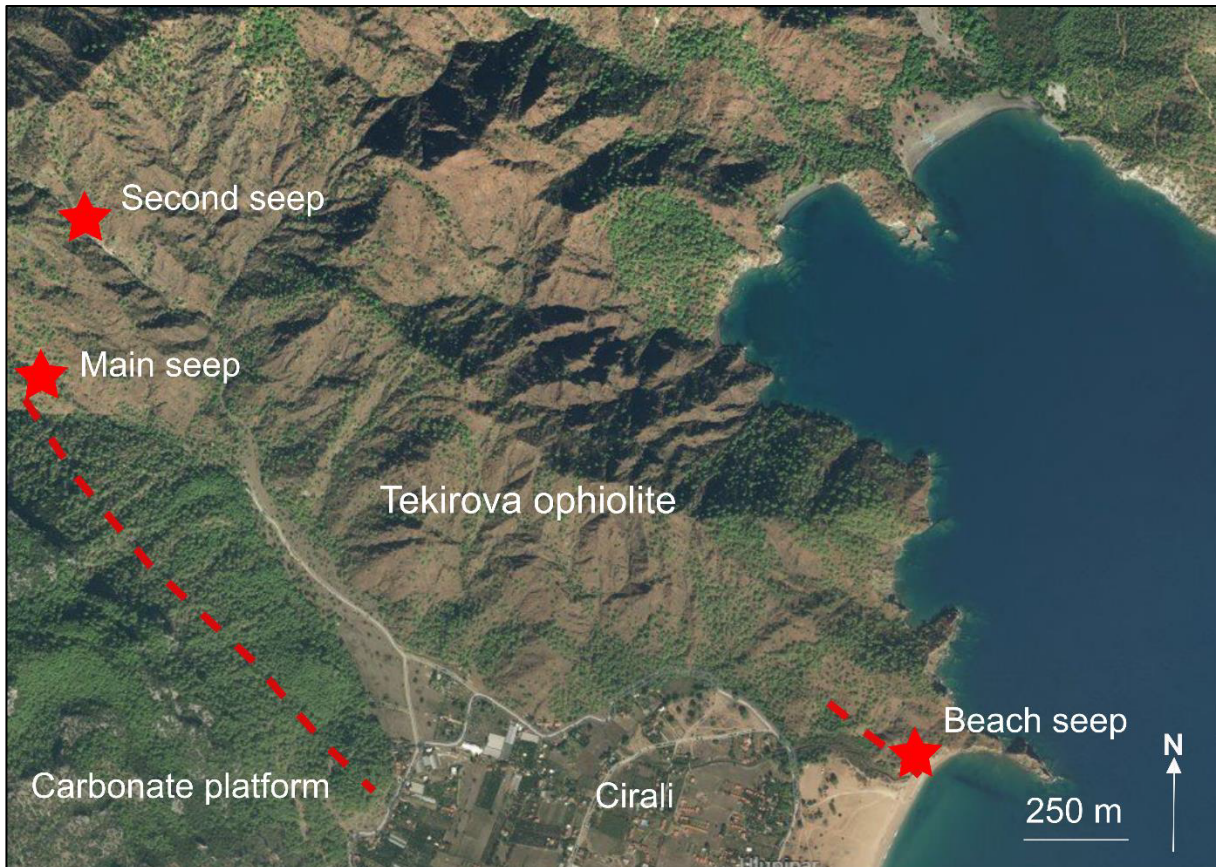


Figure 1: Map of outcrop locations, indicated by red stars. Red lines indicate fault zones separating the obducted ophiolite and the autochthonous carbonate platform. Redrawn by Rohne (2019) after Etiope et al. (2011)

<i>mineral</i>	<i>short</i>	<i>formula</i>	<i>mineral</i>	<i>short</i>	<i>formula</i>
olivine	ol	$(\text{Fe}, \text{Mg})_2[\text{SiO}_4]$	awaruite	aw	$\text{Ni}_2\text{Fe} - \text{Ni}_3\text{Fe}$
forsterite		$\text{Mg}_2[\text{SiO}_4]$	heazlewoodite	hz	Ni_3S_2
orthopyroxene	opx	$(\text{Fe}, \text{Mg})_2[\text{Si}_2\text{O}_6]$	millerite	mt	NiS
clinopyroxene	cpx	$(\text{X}, \text{Y})_2[\text{Si}_2\text{O}_6]$	pyrite	py	FeS_2
serpentinite	srp	$\text{Mg}_6(\text{OH})_8[\text{Si}_4\text{O}_{10}]$	pyrrhotite	po	FeS
brucite	bc	$\text{Mg}(\text{OH})_2$	chalcocite	cc	Cu_2S
talc		$\text{Mg}_3[(\text{OH})_2/\text{Si}_4\text{O}_{10}]$	sugakiite	sug	$\text{Cu}(\text{Fe}, \text{Ni})_8\text{S}_8$
magnetite	mag	Fe_3O_4	samaniite	sam	$\text{Cu}_2(\text{Fe}, \text{Ni})_7\text{S}_8$
calcite		$\text{Ca}[\text{CO}_3]$	bornite	bn	Cu_5FeS_4
pentlandite	pn	$(\text{Fe}, \text{Ni})_9\text{S}_8$	chalcocrite	ccp	CuFeS_2
godlevskite	gv	Ni_9S_8	covellite	cv	CuS

Table 1: Mineral names, abbreviations (if used in text or figures), and formulae. X and Y for cpx could be, among others, Ca, Na (X) and Al, Fe, Mg, Ti (Y)

Methods

All measurements and laboratory work were done at the Freie Universität Berlin.

Polarization microscopy

Twenty thin sections where looked at under polarized and reflected light, scanning for sulphide grains. Four thin sections, made from samples CS6, CS10, CS22 and CS26 were found to contain enough sulphides visible under a reflected light microscope to be analysed further. Estimated mineral composition of the four samples can be found in Table 2.

Scanning electron microscopy

The decision to use the Scanning Electron Microscope (SEM) was based on the desire to observe textures on a nm- μm scale and at least qualitatively describe chemical composition of the sulphides without destroying the textures. An SEM can provide high spatial resolution surface images and compositional analysis in a non-destructive manner. Good explanations are given in the works of *Goldstein et al.* (2017) and *Reed* (2005), which are the sources for the information on both scanning electron microscopy and electron microprobe analysis in the following paragraphs and this thesis.

The scanning electron microscope

In principle, scanning electron microscopy utilises the interaction of matter with a focussed electron beam, to provide very high-resolution greyscale images of a sample surface, the greyscale representing relative amounts of measurable signal. The electrons are emitted by a filament, usually made of tungsten, which is heated electrically for thermionic electron emission or sharply bent and exposed to a strong electrostatic field for field emission (e.g. Murphy and Good 1956). They are then accelerated towards the sample and focussed in the beam column using magnetic electron lenses. Images are created by moving the beam over a tube TV-like raster.

The beam, when hitting the surface, has a certain interaction volume within which the detectable signals are generated. The size of this interaction volume depends on the average atomic number of the material and the beam parameters, such as the incident electron energy E_0 in keV, the beam diameter or spot size in μm or nm, and the beam current in nA. When using the SEM, it is desirable to keep the interaction volume within the material you are trying to describe to avoid misleading or mixed measurements. In case of this thesis, the interaction volume had to be kept small to accommodate for the very small size of the measured sulphides, ranging from 10 to about 100 μm in grain diameter. A special interest was also on the areas close to the grain boundary, which are likely to be very thin.

An electron beam hitting a material generates backscattered electrons, secondary electrons, and characteristic as well as continuous X-rays. Both backscatter (BSE) and secondary (SE) electrons can be used to generate images. SE imaging uses the relatively low-energy secondary electrons generated by the beam, which only exit the sample if they are within a few nanometres of the surface and can be used to generate topographic images of the sample surface. BSE images give information on the relative atomic number (Z) in a sample, as elements with a higher Z have a higher chance to deflect electrons at an angle above 90°, otherwise known as backscattered electrons. High Z values, implied by a relatively high number of backscattered electrons per area unit, are usually represented by bright grey to white colours in BSE images.

Using the characteristic X-ray-energies generated by the interaction of electron beam and sample, qualitative assessment of chemical composition is possible with energy-dispersive-spectroscopy (EDS). When an atom is hit by an electron with energy above the so-called critical excitation energy (E_c), an

electron is removed from one of the atomic shells and the atom is ionised. If the removed electron was in a lower shell, an electron from an upper shell ‘jumps’ into the empty space, which releases energy in form of an X-ray photon, known as a characteristic X-ray. The energy of the X-ray photon is characteristic for the jump from one shell to another in one element, meaning there are multiple characteristic X-ray energies for all elements with enough electrons. For an element to produce a characteristic X-ray, there needs to be at least one electron in the L shell. Thus, H and He cannot produce characteristic X-rays, and other elements with low atomic number are also difficult to detect as the energies of the characteristic X-rays are very low. The characteristic X-rays with the lowest energies are those where an electron jumps from the L to the K shell, and are called $K\alpha_1$ and $K\alpha_2$, depending on the L-subshell previously occupied. These are usually sufficient when measuring elements below atomic number 30.

There is also a continuous X-ray spectrum generated by the electron beam, which occurs as an indication of electrons being slowed down statistically by interaction with nuclei and releasing energy in the process. EDS detectors collect signals over the entire energy spectrum, so removing the background created by the continuous X-rays is important for evaluation of data. An easy way to properly distinguish between continuous and characteristic X-rays is a long measurement time, through which the statistical character of the continuous spectrum is easily visible and characteristic peaks stick out nicely.

Another relevant effect in X-ray analysis is fluorescence, which occurs when the characteristic X-ray energy of one element is above the critical excitation energy of another and they appear together in a sample. This leads to more excitation in the lower energy element and therefore a larger number of detected signals (counts). X-rays can also be absorbed in the sample before reaching the surface and thus go undetected.

Sample preparation and measurements

To assure conductivity of the thin sections and avoid excessive sample heating, they were coated with carbon vapor in a sealed vacuum. The SEM used was a Zeiss Sigma 300 VP Field Emission SEM, with a Zeiss Gemini Column. As the goal of the SEM-measurements was to identify and describe sulphides, BSE rather than SE images were used predominantly in this thesis and created with the high definition backscatter detector fitted into the SEM. Since sulphides usually have a higher average atomic number than silicates, they are easy to spot in BSE images. All relatively bright areas on the BSE images of the samples were identified as potential sulphides and then checked by EDS.

As the sulphides that were looked at were very small in 2D and presumably 3D, the interaction volume had to be kept low to avoid measuring the material in which the sulphides are embedded. Therefore, E_0 was kept low, while it still had to be high enough to excite characteristic X-rays of all relevant elements. The beam was operated at an incident electron energy of 20 keV on the SEM.

The process of identifying sulphides in the grains involved first scanning all the samples for phases that appear bright in BSE-images, then taking EDS-measurements using the two Bruker Quantax Xflash 600mm² SSD EDS detectors built into the SEM on spots in all the bright phases. If sulphur was detected in the grain, it was imaged again using BSE, but at a higher resolution, with spot sizes of 100 or 10 nm, depending on whether the grains displayed textures of interest. These images were created in the Zeiss ATLAS software. In addition to spot measurements, EDS can also be applied to create element distribution maps of areas, which was done for 12 grains in total. The grains were chosen according to them having very distinct textures, unusual element contents, or element zonation.

Using the Bruker Esprit Software (Version 2.1.2), qualitative element maps were created for the 12 grains, with mapping durations ranging from 1h to 5h. The elements mapped were Fe, Ni, S, O, Mg and Si. For some grains, the software also locally identified trace concentrations of Co, Cu, Al, or Ca, which were also mapped for the respective grains. For several small areas on the maps, semi-quantitative data was extracted, but later replaced by electron-microprobe data. Detection limit should be around 0.1 wt% for major elements.

Electron microprobe

To back up the qualitative and semi-quantitative results from the SEM with quantitative analyses, point measurements were also taken through electron microprobe analysis (EMPA).

An electron microprobe (EMP) is similar to an SEM, but optimised for compositional analysis rather than imaging. It also uses a focussed electron beam to excite SE, BSE, and X-rays, generated by a tungsten filament and focussed in a column fitted with magnetic electron lenses. In addition to energy dispersive spectroscopy, which gives qualitative and semi-quantitative results, EMPs are usually fitted with wavelength-dispersive spectrometers (WDS) for quantitative analysis. These use the wavelength of the characteristic X-rays rather than their energy, with only one wavelength being measured at a time instead of the whole spectrum. The spectrometers contain analyser crystals that can be moved into position to diffract X-rays of a specific wavelength into the detector.

Each element to be quantified has one or more characteristic X-ray peaks measured in a standard of known composition, after which the same peaks are measured in the sample. This is done by measuring the intensity on the peak-wavelength and on wavelengths to the left and right of the peak as background. The net intensity is then calculated from the difference between background and peak intensity.

The peak intensity of standard and sample is not entirely proportional to element content in wt%, due to the effects of average atomic number (Z), absorption of X-rays (A) and X-ray fluorescence (F), which behave differently in materials of different composition. So called ZAF-correction is one of the methods generally used to account for these effects, and the one used on the measurements taken for this thesis.

Using a JEOL JXA 8200 Superprobe, quantitative measurements using WDS were taken on all the sulphides, measuring Fe, Ni, S, Co, Cu, As, Zn, and Pb. Even though As, Zn, and Pb were detected in trace amounts, never above 0.2 wt%, the relative errors of at least 60% lead to the decision to disregard these elements in the evaluation.

The beam was running at a beam current of 20nA, with an incident electron energy of 15 keV and a beam diameter of 1 μ m. The lower keV compared to the SEM was chosen here because an already established setup on the EMP was used and it is best to change as few parameters as possible when doing that. Keeping the interaction volume low was also relevant to only measure the desired areas and nothing else. WDS measurements were taken for 10s on peak and 5s per side for the background. The detection limit is estimated around 0.03-0.06 wt%, the analytical error was below 0.25 wt% for all measurements, except for the above-mentioned elements. Only measurements with a total of 100 ± 2 wt% were taken into consideration for plots and quantitative statements. All measurements and errors are listed in Appendix table 1.

Results

General sample composition

The thin sections main components (Table 2) are serpentine, mostly in typical mesh structure, olivine, and pyroxenes, mostly clinopyroxene. All samples show the typical serpentine mesh texture, locally the replacement of olivine is not completed and it is still present in the mesh cores. Pyroxene is either replaced by serpentine forming bastites or still present in the samples. They occasionally contain amphiboles, talc and calcite. Opaque phases are spinells, iron oxides and sulphides.

<i>thin section</i>	<i>srp</i>	<i>ol</i>	<i>cpx</i>	<i>opx</i>	<i>amph</i>	<i>opaque</i>
CS6	85%	5%	5%	-	<5%	<5%
CS10	70%	10%	10%	5%	-	5-10%
CS22	90%	<5%	<5%	-	-	<5%
CS26	30%	60%	5%	<5%	-	<5%

Table 2: Mineralogy of the samples, estimated from polarization microscopy, in vol.-%

Overall sulphide content

The sulphide content is below 0.5 vol% in all the samples. The sulphides occur in different surroundings, some within the serpentine mesh, some in veins, occasionally in direct contact to olivine (Table 3). The number of sulphide grains per section is in single digits. The sulphides are mostly pentlandite and millerite, some are partly heazlewoodite, godlevskite, chalcocite (with about 3-4 at% Fe), sugakiite, or samaniite (Fig. 2). Some of the pentlandite contains small amounts of Co, the highest being around 6 at% (CS22_R13_1). The 12 grains can be split into the following groups (Table 3):

1. Pentlandite with μm -scale areas of awaruite
2. Pentlandite with reaction zones that are part fibre-like, part awaruite
3. Pentlandite with magnetite and sometimes elevated Cu contents
4. Lightly broken up pentlandite

Notably, this also splits the 4 samples into 2 groups, either containing awaruite as a presumed product of alteration (CS6, CS22), or having small amounts of Cu in the sulphide phase and magnetite intergrown with the sulphides (CS10, CS26). A trend from pentlandite to awaruite along 25 at% Fe is implied when plotting the compositions in a ternary (Fe, S, Ni + Co + Cu) diagram (Fig. 2A), most likely due to mixed analysis in very small grained mineral intergrowths.

gr.	grain	assemblage	surr.
1	CS6_R61	pn + aw	srp
	CS6_R71	pn + aw	srp
	CS22_R13_1	pn*/gv + mt + aw	srp vein
	CS22_R13_2	pn/gv + mt + hz + aw	srp vein
	CS22_R21	pn* + aw	srp
2	CS6_R72	pn* + aw + fibre	srp + ol
	CS6_R73	pn* + aw + fibre	srp
3	CS10_R14	pn + mag	srp
	CS10_R32	pn + mag	srp
	CS26_R14	pn + sug + sam + mag + cc	srp + ol
	CS26_R16	pn + (sug)	srp + ol
4	CS26_R10	pn	ol

Table 3: Sulphide grains, their mineral assemblage and surrounding materials. pn marked with a * has >2 at% Co. gr. = group

Figure 2 A: Ternary plots of all EMPA measurements with stoichiometric compositions as orange stars for Fe-Ni-Co-sulphides. See Table 1 for abbreviations. Filled diamonds represent the presence of Co, Cu, or both, according to legend. Data in Appendix Table 1

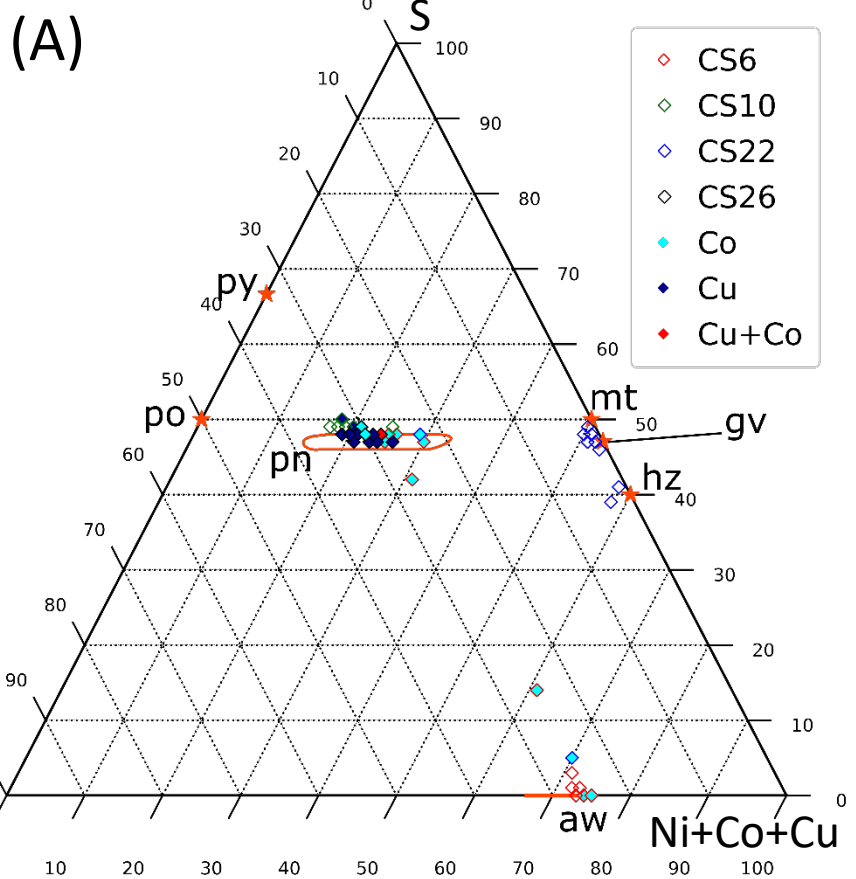
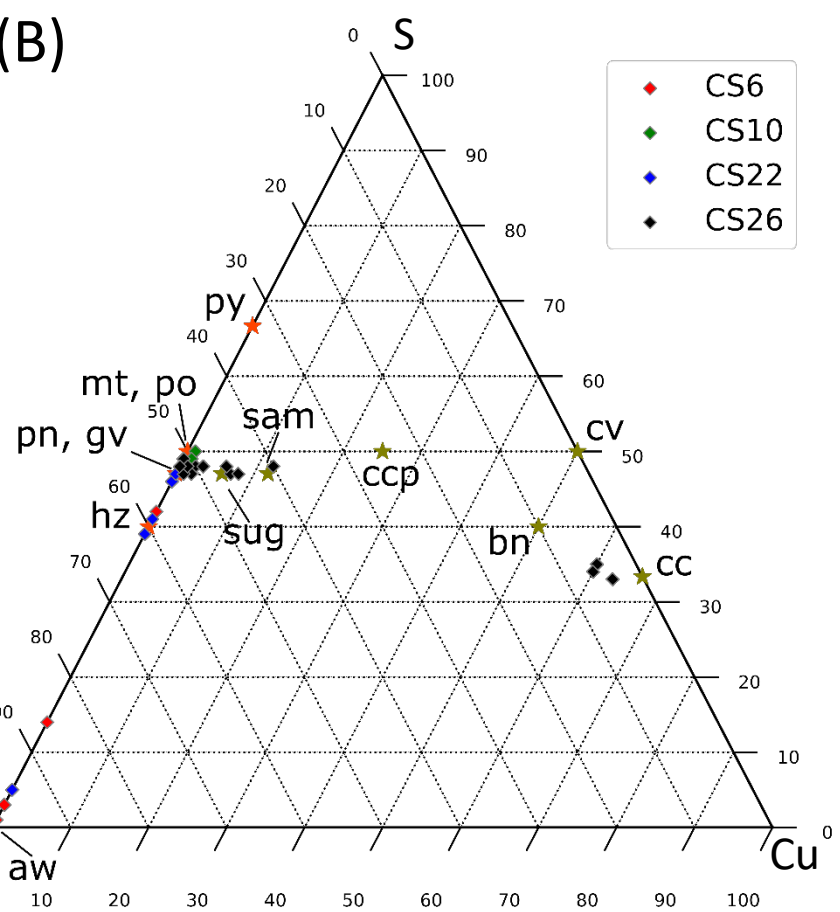


Figure 2 B: Ternary plots of all EMPA measurements with stoichiometric compositions as orange stars for Fe-Ni-Co-sulphides and olive stars for Cu-bearing sulphides. See Table 1 for abbreviations. Chalcocite occurs only with small Fe contents (3-4 at%). Data in Appendix Table 1



Observations in the grains

1. Pentlandite with a μm -scale rim of awaruite

The most common sign of alteration based on the sulphide mineralogy observed in the samples is the appearance of awaruite ($\text{Ni}_{2.3-2.88}\text{Fe}$) with pentlandite or millerite (Fig. 3). Awaruite-areas are largest around pentlandite. Another observation to be made is the absence of magnetite, which would be expected following reaction (V). The grains of CS22 have elevated Ni contents, containing millerite, godlevskite and heazlewoodite. Grains CS22_R13_1 and 2 vary a lot in composition between different Ni-sulphides and also contain some Ni-oxide, according to the EDS-maps (Appendix fig. 1, 2, 7, 8, 9).

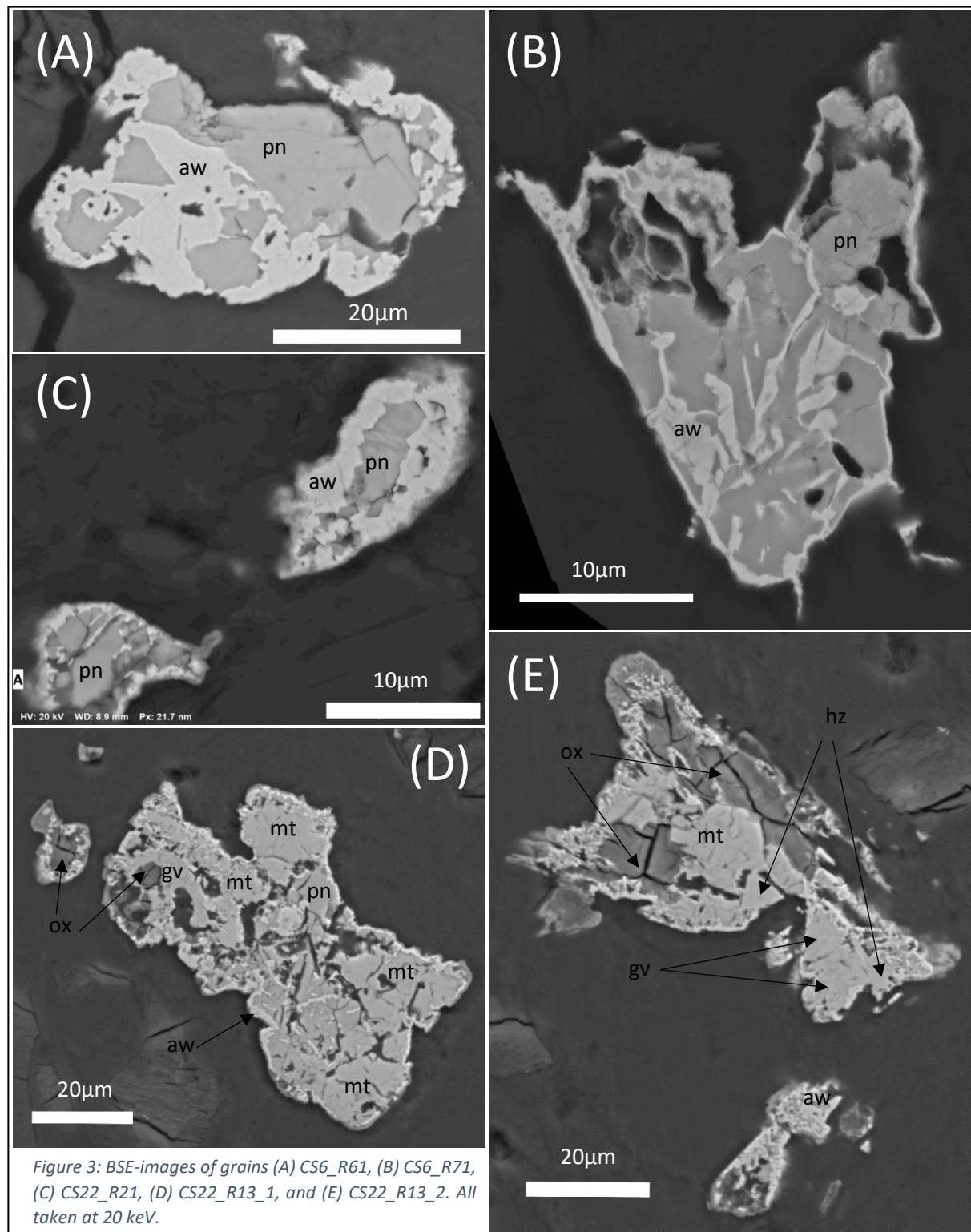


Figure 3: BSE-images of grains (A) CS6_R61, (B) CS6_R71, (C) CS22_R21, (D) CS22_R13_1, and (E) CS22_R13_2. All taken at 20 keV.

2. Pentlandite with reaction zones that are part fibre-like , part awaruite

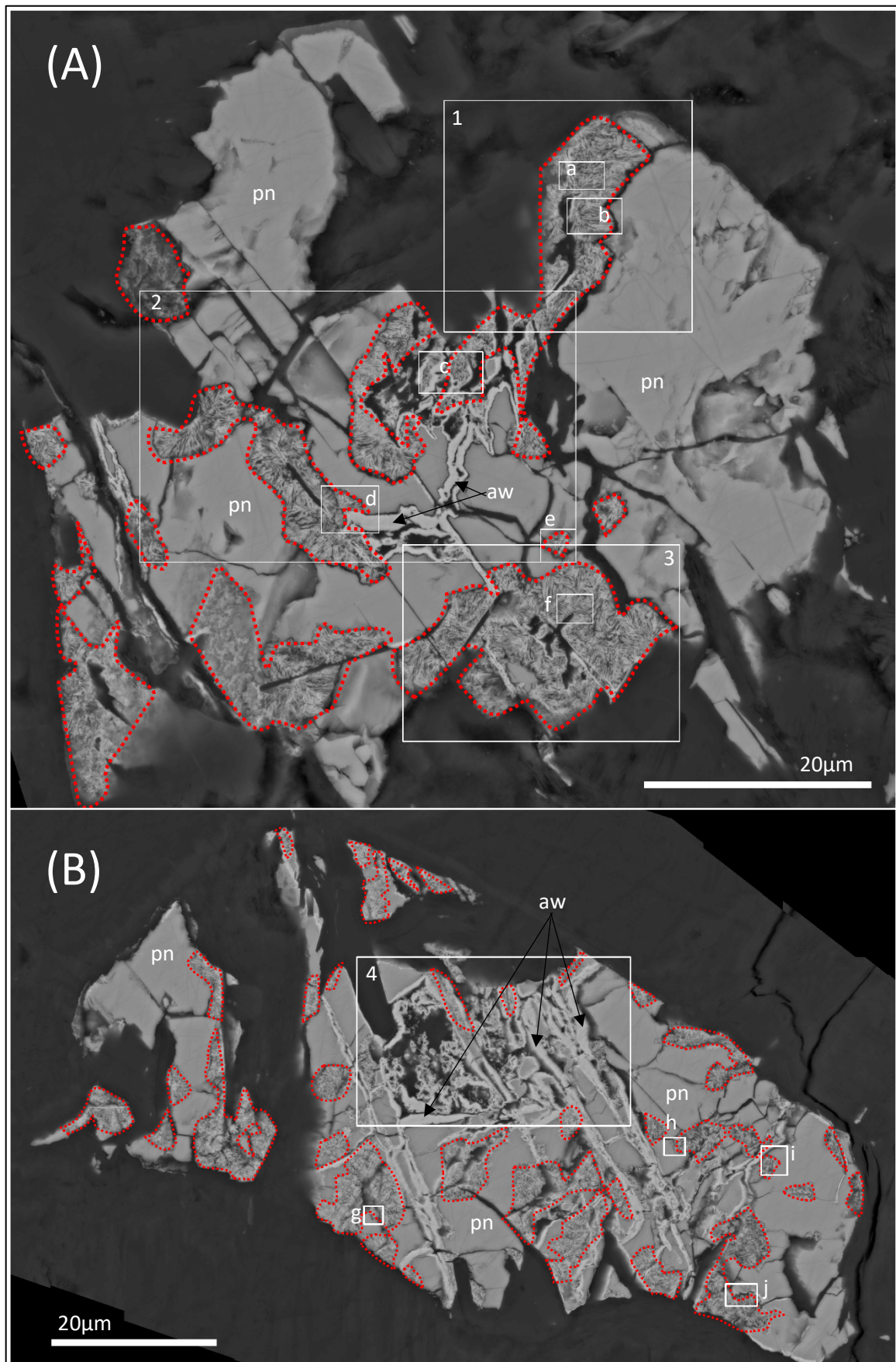
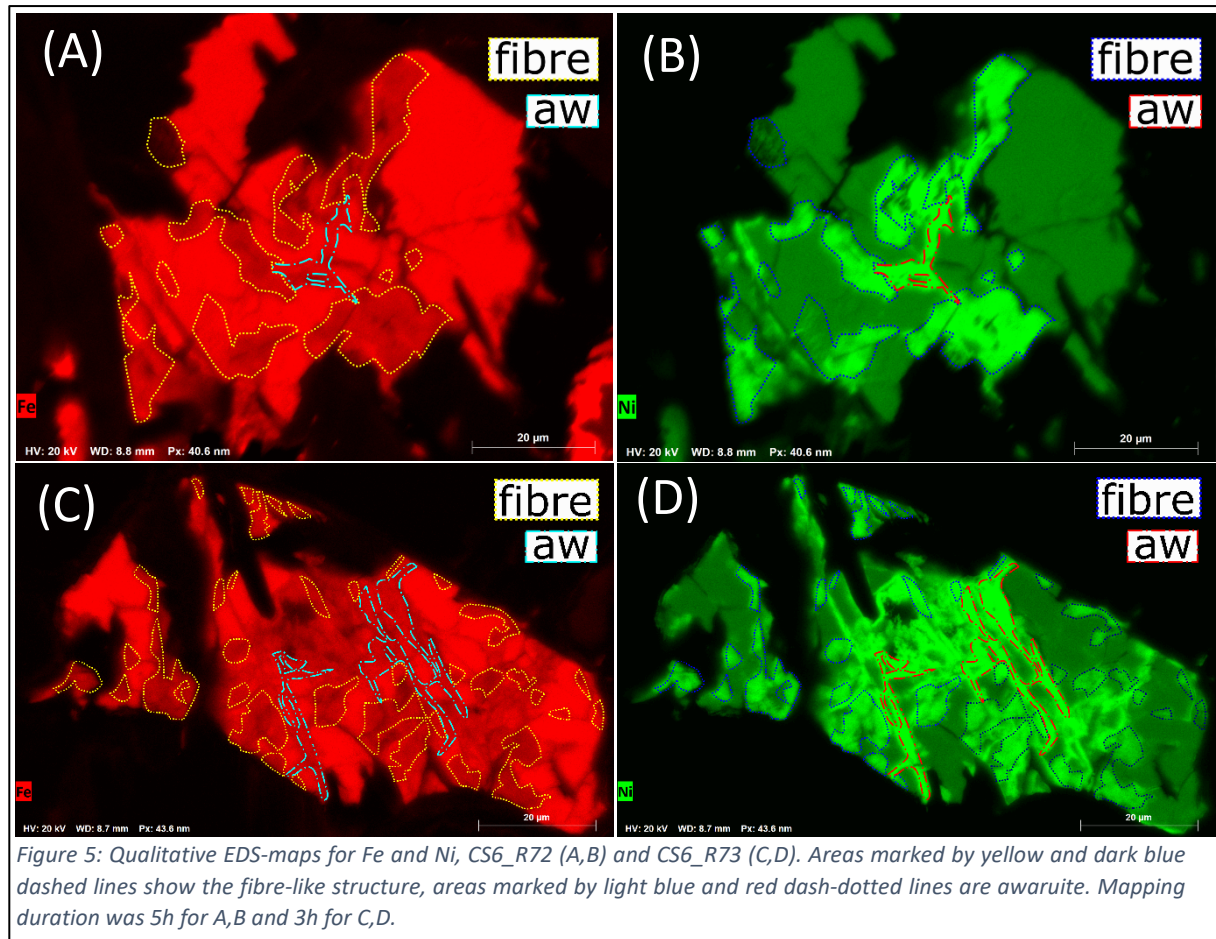


Figure 4: BSE images of (A) CS6_R72 and (B) CS6_R73. Red dashed lines are areas that show fibre-like structure. Detail images 1-4 are found in Figure 6, a-j in Figure 7. Images taken at 20keV

The two grains of group 2 show particularly interesting textures. Detailed BSE-images are shown in Figure 4. Both grains are mostly pentlandite, with the approximate stoichiometric formulas being $\text{Fe}_{4.52}\text{Ni}_{3.68}\text{Co}_{0.45}\text{S}_8$ (Fig. 4A) and $\text{Fe}_{4.74}\text{Ni}_{3.6}\text{Co}_{0.36}\text{S}_8$ (Fig. 4B). They also contain some awaruite (ca. $\text{Ni}_{2.75}\text{Fe}$). Some crystallographically oriented monosulphide-solid-solution (mss) exsolution lamellae can be observed in the pentlandite (Fig. 4A, Fig. 6.1, on the right side in both), which likely formed during cooling (Craig 1973; Durazzo and Taylor 1982a). Additionally, the grains contain areas with a fibre-like structure (red dashed lines in Fig. 4) of intergrown bright phases, presumably Fe-Ni-alloy, and darker phases, where the sulphide has been replaced by silicate phases or where a mineral phase was removed during sample preparation. These areas seem to be replacing the pentlandite, are usually connected to a grain boundary, and can reach deep into the pentlandite.

The small size of the lamellae, with widths of 30-200nm, makes it impossible to determine the exact composition through SEM or EMPA, with EMPA measurements only yielding totals of 40-60 wt.%, with a relative composition of awaruite. Qualitative assessment is possible using the EDS maps in Figure 5. The areas in which the fibres are visible are enriched in Ni, compared to the host pentlandite. On the other hand, Fe is more abundant within the intact pentlandite compared to the fibrous area (Fig. 5). EDS-maps for S, Si and Mg suggest that the areas contain silicate, but no sulphur (Appendix Fig. 3, 4).



The areas take different shapes, as seen in Figure 6. Sometimes they reach into the grain in almost channel-like shape, connecting to even smaller channels of awaruite (Fig. 6.2 around d), sometimes they form almost half-circles, growing inward more homogenically (Fig. 6.3, 6.2 central left) or even just an inward moving front with apparent crystallographic orientation along the boundary to the intact grain (Fig. 6.1). Intergrowths with or at least in contact to awaruite are common (Fig. 6.2, 3, 4), but not always present.

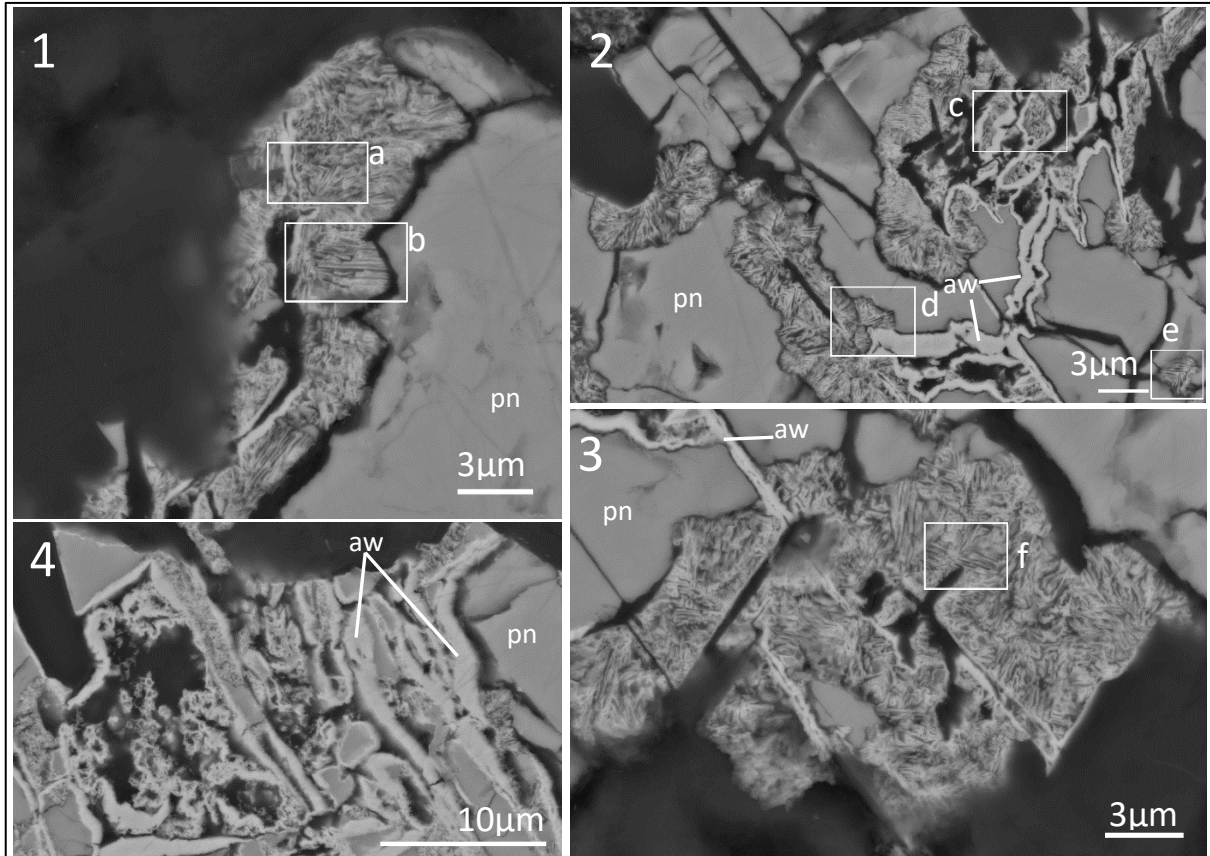


Figure 6: Detail images of CS6_R72 (1-3) and CS6_R73 (4). Taken at 20 keV. Darkest grey is silicate, lighter grey pentlandite and bright phase awaruite.

High resolution BSE-images of the fibre-like texture (Fig. 7) show that they contain a very bright phase, similar in average atomic number to the awaruite, and a darker phase, similar under the electron microscope to the material surrounding the grain, which is serpentine for R73 and mostly serpentine and some olivine for R72. The bright and the dark phase are closely intergrown as small bars or lamellae, less than half a μm wide, sometimes even down to 30nm. In some areas, there are perpendicular textures of intergrown bright and dark phase (Fig. 7a, e, f, h). Some of the areas displaying the texture are surrounded by awaruite (Fig. 7c). Most of the time, the orientation is very localized to areas of $2 \times 2 \mu\text{m}$ at the largest and does not connect to the adjacent material. Areas without orientation usually do not contain elongated lamellae, instead displaying small dots or blebs of the bright phase without any particular shape, difficult to tell apart even on the highest resolution achieved during the measurements (e.g. Fig. 7g, i).

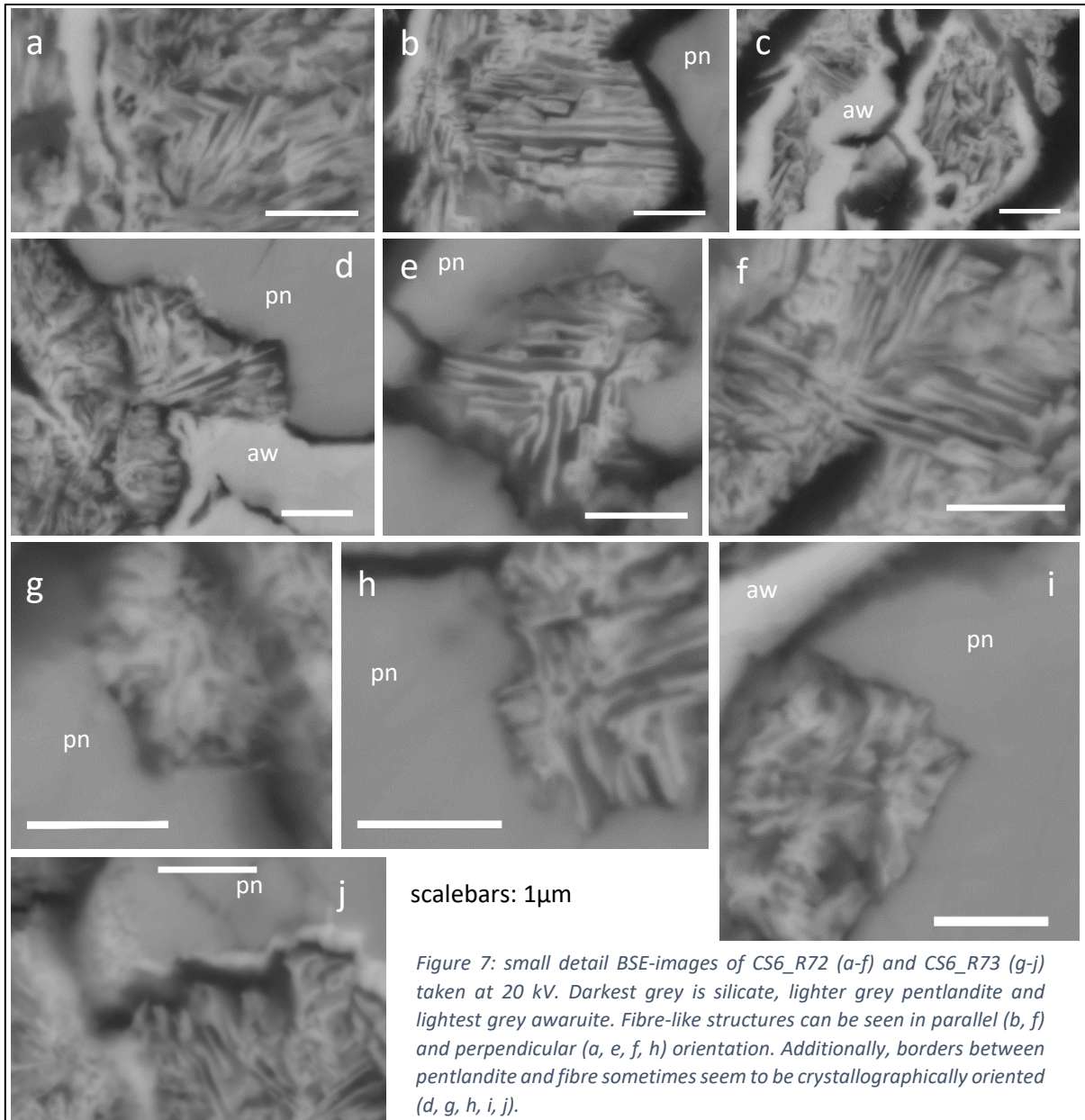


Figure 7: small detail BSE-images of CS6_R72 (a-f) and CS6_R73 (g-j) taken at 20 kV. Darkest grey is silicate, lighter grey pentlandite and lightest grey awaruite. Fibre-like structures can be seen in parallel (b, f) and perpendicular (a, e, f, h) orientation. Additionally, borders between pentlandite and fibre sometimes seem to be crystallographically oriented (d, g, h, i, j).

3. Pentlandite with magnetite and sometimes elevated Cu-contents

The third group of sulphides do not show the fibre-like intergrowth of silicate and presumed awaruite (Fig. 8). They all contain areas with enough Cu to be detected by the EDS-mapping (Fig. 9), though the grains in CS10 (A and C in Figs. 8, 9) only contain supposed Cu in areas where the grain has morphological features. Since EMPA analysis could not confirm the occurrence of Cu in most places, the qualitative maps for CS10 can at best be taken as an indication for very low concentrations of Cu, though elevated in respect to the surrounding grain.

Except for CS26_R16 (Fig. 8B, 9B), the grains are partly and pseudomorphically replaced with magnetite. Cu mostly appears within pentlandite, though some measurements yield chalcocite, sugakiite, or samaniite (Fig. 8D, 9D). In CS26_R16 (Fig. 8B, 9B), Cu is concentrated in a corner of the grain where there seemingly used to be pentlandite, with it now being mostly silicate. CS26_R14 (Fig. 8D, 9D) shows crystallographically oriented lamellae with elevated Cu-contents, which might even be native Cu, though no area big enough to be measured by EMPA was found. The grain contains the highest amount of Cu found in the samples.

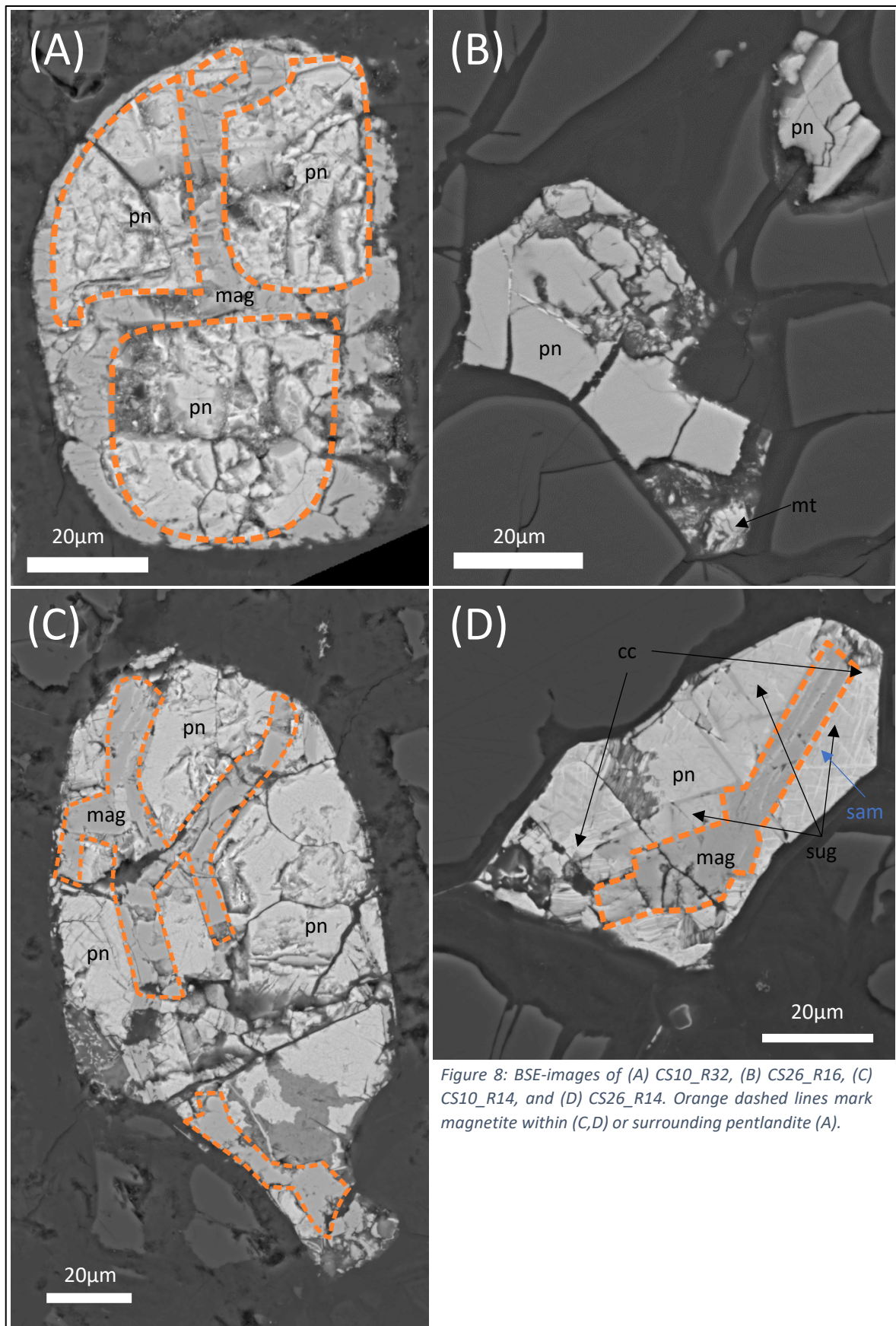


Figure 8: BSE-images of (A) CS10_R32, (B) CS26_R16, (C) CS10_R14, and (D) CS26_R14. Orange dashed lines mark magnetite within (C,D) or surrounding pentlandite (A).

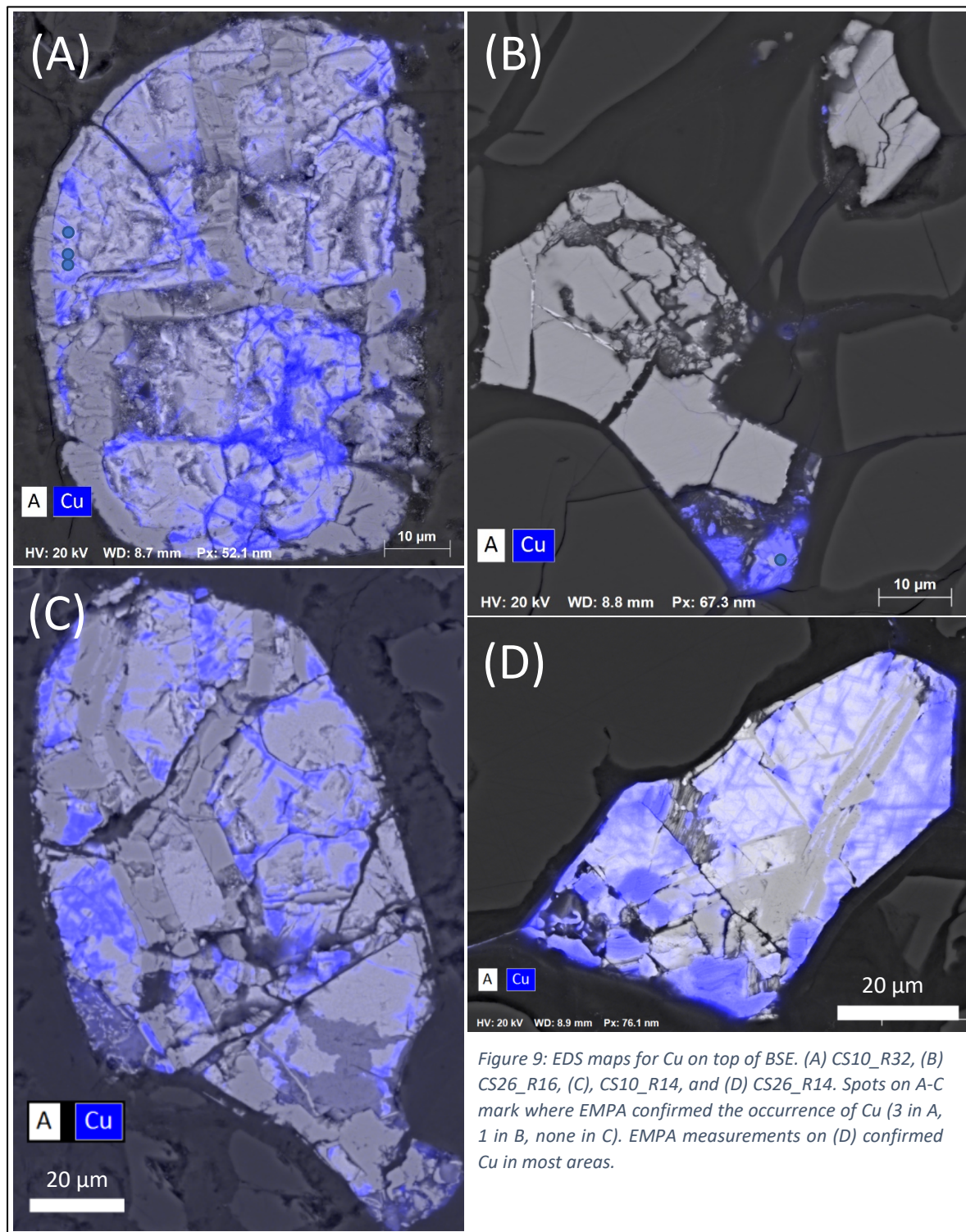


Figure 9: EDS maps for Cu on top of BSE. (A) CS10_R32, (B) CS26_R16, (C), CS10_R14, and (D) CS26_R14. Spots on A-C mark where EMPA confirmed the occurrence of Cu (3 in A, 1 in B, none in C). EMPA measurements on (D) confirmed Cu in most areas.

4. Lightly broken up pentlandite

This group, consisting of only one grain, represents most of the sulphides that were found in the thin sections, with no distinct textures or odd elemental distribution. A BSE image of the grain is displayed in Figure 10. Mapping duration for the EDS-map was limited to 30 minutes due to the lack of textures relevant to this thesis. The grain has some cleavages, the gaps being filled with silicate. Other than that, it is simply pentlandite with a composition of roughly $\text{Fe}_{5.3}\text{Ni}_{3.3}\text{Co}_{0.07}\text{S}_8$.

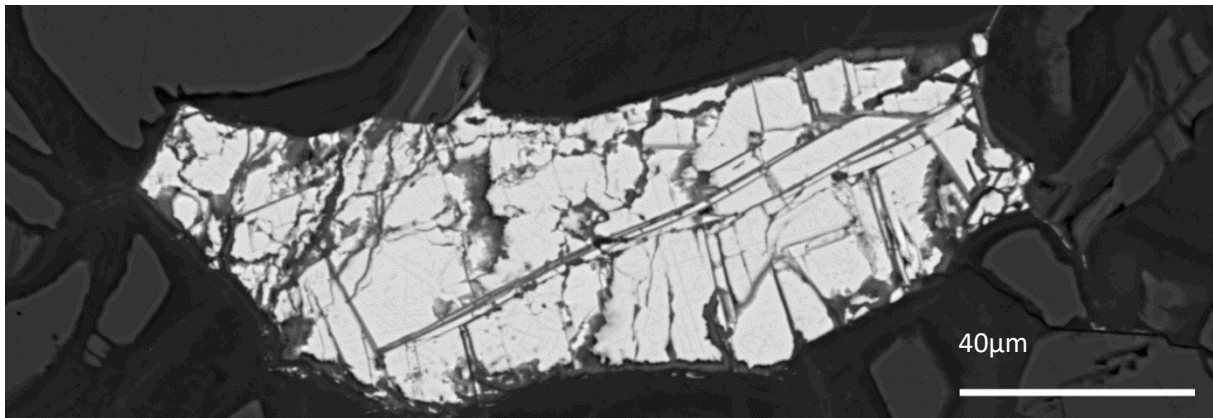


Figure 10: BSE-image of grain CS26_R10, making up group 4. Note that the brightness and contrast settings are very different in this image compared to the other groups, making the pentlandite very bright in this image.

Discussion

Sulphide micro- and nanotextures

There are several different microstructures and exsolution textures described for Fe-Ni as well as Fe-Cu-sulphides. Several studies covering cooling exsolution experiments have been conducted and show the different ways in which a monosulphide-solid-solution (mss) exsolves into different sulphides during cooling (Durazzo and Taylor 1982a; Durazzo and Taylor 1982b; Craig 1973). For example, crystallographically oriented lamellae of stoichiometric pentlandite within mss, formed during cooling, were observed by *Craig* (1973) and *Durazzo and Taylor* (1982a). Similar observations have been made for Fe-Co-sulphides (Farrell and Fleet 2002). Experiments show that these lamellae are randomly oriented in rapidly cooled samples (Francis et al. 1976), thus allowing for a qualitative assessment of the cooling rate. There have also been studies on microtextures of sulphides in meteorites (Harries and Langenhorst 2013) and Cu-(Fe)-sulphides from ore deposits (Ciobanu et al. 2017).

These studies, however, are all focused on the exsolution of sulphides from melt or a primary solid-solution, and do not cover alteration processes. *Hidalgo et al.* (2020) reported on experiments with Cu-sulphides in acidic solution, and observed different textures and reactions resulting from dissolution of metals from the sulphides. Still, this does not cover the rare conditions under which serpentinization takes place, which dissolve sulphur and not metals from the sulphides. Especially during low temperature serpentinization, conditions are often highly alkaline rather than acidic, with the pH between 9-11 or even higher (Janecky and Seyfried 1986). Comparing the textures seen after alteration through a highly reducing fluid to those known from earlier works, may help to understand the processes that sulphides in peridotites are subject to during serpentinization.

Primary and secondary minerals

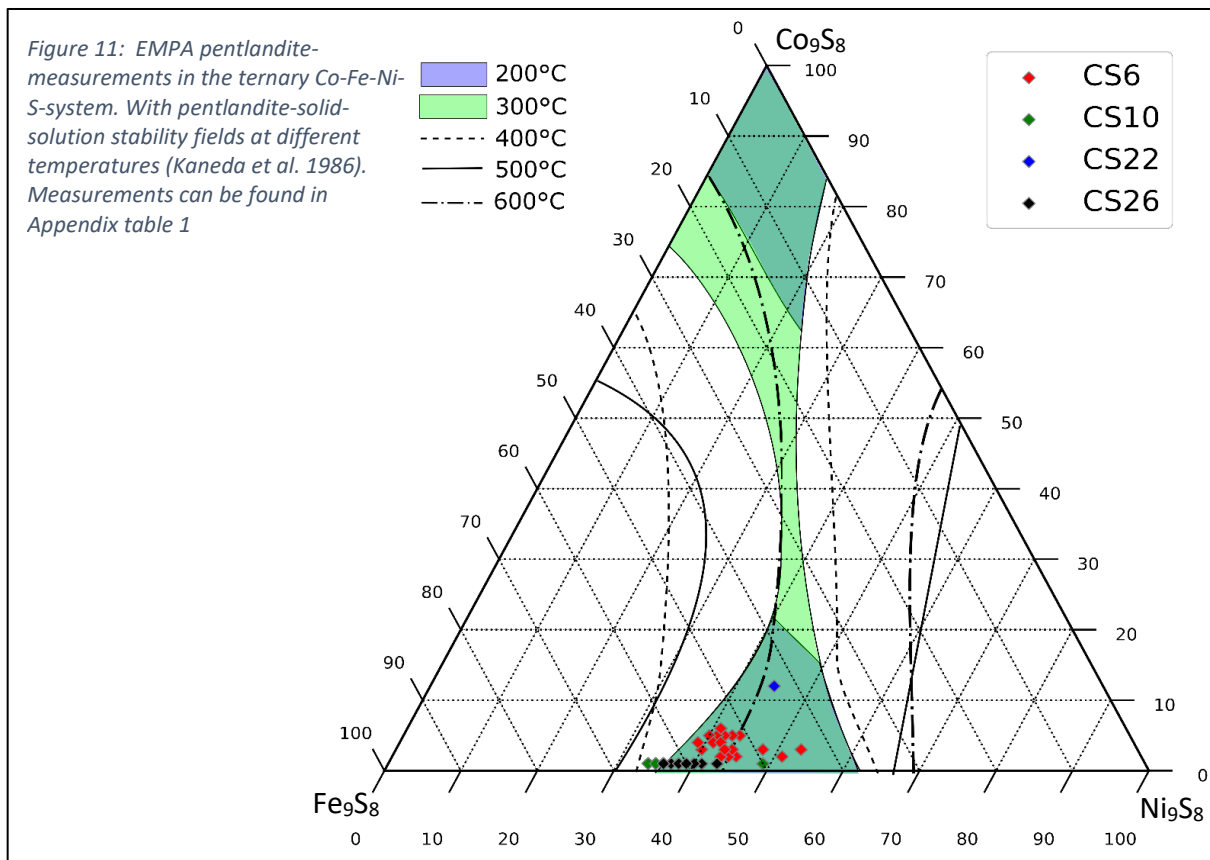
It is likely that the rocks at the Chimaera seep have undergone at least two phases of hydrothermal alteration, one at the ocean floor and one still ongoing on land with meteoric water as the main fluid source. Zwicker *et al.* (2018) identified two generations of brucite in the rocks and estimated a temperature of 200-300°C for one phase of serpentinization, and temperatures below 200°C for another. Etiope *et al.* (2011) estimated a present-day serpentinization temperature of 50-100°C and described the emitted gas to be composed mainly of methane (~87%) and hydrogen (~10%).

Klein and Bach (2009) described (Co)-pentlandite in serpentized peridotites with reaction rims of awaruite, sometimes with magnetite, similar to the grains in group 1 and 3. They did not report on any Cu-bearing sulphides or the textures shown by grains in group 2. This leads to the assumption that group 1 shows the reactions that took place during the fluid-rock interaction on the ocean floor, while group 2 displays the dynamics of the still ongoing alteration by meteoric water. Group 3, containing small amounts of Cu that are not likely to have originated in the unaltered peridotite, may be indication of another, Cu-bearing, fluid interacting with the rocks, similar to the suggestions of Schwarzenbach *et al.* (2014) in another ophiolite. On the other hand, since there is only a single grain with Cu-sulphides, assumptions here are highly speculative and the Cu might be of different origin.

Using the composition of sulphides to estimate alteration conditions

Using the composition of Co-bearing pentlandite, it is possible to determine a range of temperature within which it was formed (Kaneda *et al.* 1986).

All pentlandite-measurements with no or very low Cu-contents have been plotted in Figure 11, with stability fields marked after Kaneda *et al.* (1986). Overall, the measurements do fit into the 200-300°C range proposed by Zwicker *et al.* (2018), leading to the assumption that the still intact pentlandite precipitated during the first stage of alteration, probably enabled through seawater-rock interaction.



Phase relations in the Fe-Ni-Co-O-S-system can also help to estimate activities and fugacities of H₂S and H₂ during the alteration process. Using the activity-activity phase diagrams calculated by *Klein and Bach* (2009), it is possible to determine a relatively small window of activities for both H₂S and H₂, since the stability field of awaruite grows smaller with decreasing temperature. For the proposed first stage of alteration at 200-300°C, the occurrence of awaruite requires a(H₂S) to be 10⁻⁴ or lower, and a(H₂) to be 10⁻²-10⁻¹ or higher (see *Klein and Bach* (2009) for phase diagrams). This first event may also have not produced any awaruite, which could all be produced in the later stages of alteration. This would increase the window of activities for the first stage significantly.

The lowest temperature for which calculations were made by the authors is 150°C. Using that phase diagram (Fig. 12) and the assumption that the trend for the stability field of awaruite continues with decreasing temperature, a(H₂S) would need to be below 10⁻⁶ and a(H₂) above 10⁻² in the reaction that is currently producing awaruite at temperatures of 50-100°C. All of this does not consider the presence of large amounts of methane in the reaction fluid, though it could be argued from the resulting assemblage that methane remains inert or acts as a reducing agent, similar to H₂. A suggestion for the window of activities the reactions are currently in is marked in red in Figure 12.

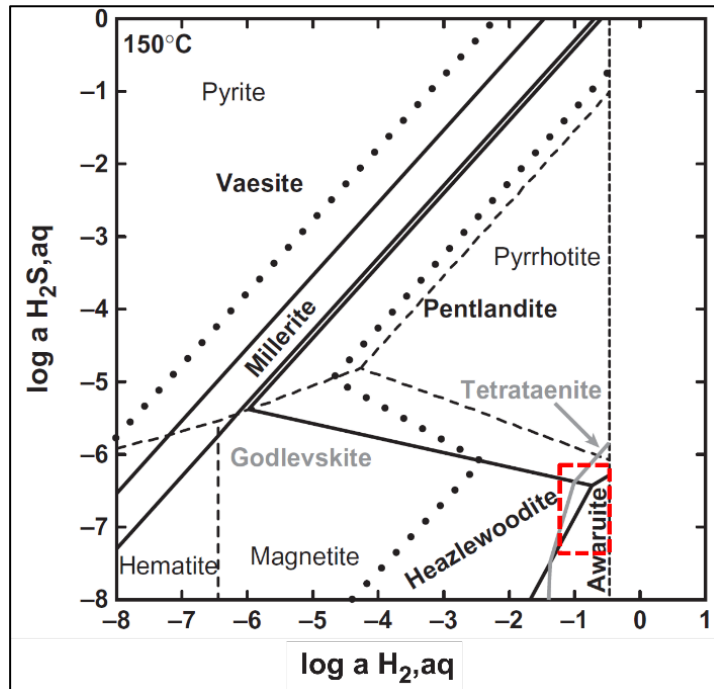


Figure 12: Activity/activity-diagram for H₂S and H₂, with phase stability fields of the Fe-Ni-O-S system (*Klein and Bach* 2009)

The occurrence of millerite, heazlewoodite and godlevskite in CS22_R13_1 and 2 indicates a much lower a(H₂) at some point in those samples, and since they also contain some Ni-oxide, the reactions leading to this compositions may have taken place on the surface or close to it.

Interpreting the fibre-like texture in the grains of group 2

The mineralogy of the textures (Figs. 4, 6, 7) is presumed to be awaruite as the bright lamellae, and Mg-silicate (serpentine, forsterite/olivine) as the dark material around it, judging from the greyscale of the BSE-images and the analysis of areas of equal grey-value. As the textures always appear in places where there likely was pentlandite before, the reaction probably followed a mechanism similar to reaction (V) in removing H₂S from the mineral, though the lack of magnetite in the grains may require a different reaction path and the presence of methane needs to be taken into account.

Since the described textures often show some orientation, it is hypothesized that sulphur is removed from the crystal structure, leaving empty spaces which are then filled with silicate unless the remaining Fe and Ni recrystallize as solid awaruite, which is observed in coexistence with the fibre (Fig. 4), but also without it in group 1 (Fig. 3).

Assumptions on reaction mechanisms and processes on the crystallographic scale are highly speculative and would require further research and experiments on the effect of methane-enriched and hydrogen-bearing fluids on sulphides.

Conclusion

The observations made in the samples give insight into the conditions of past and present serpentinization events under highly reducing conditions. The reaction from pentlandite to awaruite is documented well, and in combination with the composition of the pentlandite, affirms previous assumptions about the past serpentinization temperature between 200 and 300°C. The stability of awaruite in the current system of serpentinization with meteoric waters indicates H₂-activities above 10⁻² and H₂S-activities below 10⁻⁶. The exact influence of methane, which is the main component in the gas emitted from the seep (Etiope et al. 2011), could not be derived from the samples but it is argued that the resulting assemblage of pentlandite and awaruite indicates the methane to either be inert or similar in effect to H₂ in the reactions.

The textures that are created during the extraction of sulphur from the pentlandite to produce awaruite can be observed particularly well in two grains (Fig. 4), with very small fibre-like intergrowths of awaruite and silicate. They show some orientation, both within the fibre-area and on the boundary to intact pentlandite (Fig. 7). It is suggested that the orientation represents crystallographic planes, meaning that sulphur is removed from the crystal structure while iron and nickel remain as awaruite lamellae before solid awaruite crystallizes or the gaps are filled with silicate.

To test these assumptions, experiments testing the effects of highly reducing and methane-bearing fluids on the stability of sulphides, especially pentlandite, are needed.

Publication bibliography

- Abrajano, Teofilo A.; Pasteris, Jill D. (1989): Zambales ophiolite, Philippines. In *Contrib Mineral Petrol* 103 (1), pp. 64–77.
- Aldanmaz, E.; Schmidt, M. W.; Gourgaud, A.; Meisel, T. (2009): Mid-ocean ridge and supra-subduction geochemical signatures in spinel–peridotites from the Neotethyan ophiolites in SW Turkey: Implications for upper mantle melting processes. In *Lithos* 113 (3-4), pp. 691–708. DOI: 10.1016/j.lithos.2009.03.010.
- Alt, Jeffrey C.; Shanks, Wayne C. (1998): Sulfur in serpentinized oceanic peridotites: Serpentinization processes and microbial sulfate reduction. In *J. Geophys. Res.* 103 (B5), pp. 9917–9929. DOI: 10.1029/98JB00576.
- Andreani, M.; Mével, C.; Boullier, A.-M.; Escartín, J. (2007): Dynamic control on serpentine crystallization in veins: Constraints on hydration processes in oceanic peridotites. In *Geochem. Geophys. Geosyst.* 8 (2), n/a-n/a. DOI: 10.1029/2006GC001373.
- Anonymous (1972): Penrose field conference on ophiolites. In *Geotimes* 17 (12), pp. 24–25.
- Bach, W.; Früh-Green, G. L. (2010): Alteration of the Oceanic Lithosphere and Implications for Seafloor Processes. In *Elements* 6 (3), pp. 173–178. DOI: 10.2113/gselements.6.3.173.
- Bach, Wolfgang; Paulick, Holger; Garrido, Carlos J.; Ildefonse, Benoit; Meurer, William P.; Humphris, Susan E. (2006): Unraveling the sequence of serpentinization reactions: petrography, mineral chemistry, and petrophysics of serpentinites from MAR 15°N (ODP Leg 209, Site 1274). In *Geophys. Res. Lett.* 33 (13). DOI: 10.1029/2006GL025681.
- Berndt, Michael E.; Allen, Douglas E.; Seyfried Jr, William E. (1996): Reduction of CO₂ during serpentinization of olivine at 300 C and 500 bar. In *Geology* 24 (4), pp. 351–354.
- Çelik, Ömer Faruk; Delaloye, Michel; Feraud, Gilbert (2006): Precise 40 Ar– 39 Ar ages from the metamorphic sole rocks of the Tauride Belt Ophiolites, southern Turkey: implications for the rapid cooling history. In *Geol. Mag.* 143 (2), pp. 213–227. DOI: 10.1017/S0016756805001524.
- Chamberlain, J. A.; McLeod, C. R.; Traill, R. J.; Lachance, G. R. (1965): Native metals in the Muskox intrusion. In *Canadian Journal of Earth Sciences* 2 (3), pp. 188–215.
- Ciobanu, Cristiana L.; Cook, Nigel J.; Ehrig, Kathy (2017): Ore minerals down to the nanoscale: Cu-(Fe)-sulphides from the iron oxide copper gold deposit at Olympic Dam, South Australia. In *Ore Geology Reviews* 81, pp. 1218–1235. DOI: 10.1016/j.oregeorev.2016.08.015.
- Craig, James R. (1973): Pyrite-pentlandite assemblages and other low temperature relations in the Fe-Ni-S system. In *American Journal of Science* 273 (A), pp. 496–510.
- Dewey, J. F. (1976): Ophiolite obduction. In *Tectonophysics* 31 (1-2), pp. 93–120. DOI: 10.1016/0040-1951(76)90169-4.
- Dilek, Y.; Furnes, H. (2014): Ophiolites and Their Origins. In *Elements* 10 (2), pp. 93–100. DOI: 10.2113/gselements.10.2.93.
- Durazzo, A.; Taylor, L. A. (1982a): Exsolution in the MSS-pentlandite system: Textural and genetic implications for Ni-sulfide ores. In *Mineral. Deposita* 17 (3), pp. 313–332.
- Durazzo, Aldo; Taylor, Lawrence A. (1982b): Experimental exsolution textures in the system bornite-chalcopyrite: Genetic implications concerning natural ores. In *Mineral. Deposita* 17 (1), pp. 79–97.

Eckstrand, O. R. (1975): The Dumont serpentinite; a model for control of nickeliferous opaque mineral assemblages by alteration reactions in ultramafic rocks. In *Economic Geology* 70 (1), pp. 183–201. DOI: 10.2113/gsecongeo.70.1.183.

Etiope, Giuseppe; Schoell, Martin; Hosgörmez, Hakan (2011): Abiotic methane flux from the Chimaera seep and Tekirova ophiolites (Turkey): understanding gas exhalation from low temperature serpentinization and implications for Mars. In *Earth and Planetary Science Letters* 310 (1-2), pp. 96–104.

Farrell, S. P.; Fleet, M. E. (2002): PHASE SEPARATION IN $(\text{Fe}, \text{Co})_1 \times \text{S}$ MONOSULFIDE SOLID-SOLUTION BELOW 450 C, WITH CONSEQUENCES FOR COEXISTING PYRRHOTITE AND PENTLANDITE IN MAGMATIC SULFIDE DEPOSITS. In *The Canadian Mineralogist* 40 (1), pp. 33–46. DOI: 10.2113/gscanmin.40.1.33.

Francis, Carl A.; Fleet, Micheal E; Misra, Kula; Craig, James R. (1976): Orientation of exsolved pentlandite in natural and synthetic nickeliferous pyrrhotite. In *American Mineralogist* 61, pp. 913–920.

Frost, Ronald B. (1985): On the Stability of Sulfides, Oxides, and Native Metals in Serpentinite. In *Journal of Petrology* 26 (1), pp. 31–63. DOI: 10.1093/petrology/26.1.31.

Goldstein, Joseph I.; Newbury, Dale E.; Michael, Joseph R.; Ritchie, Nicholas W. M.; Scott, John Henry J.; Joy, David C. (2017): Scanning electron microscopy and X-ray microanalysis: Springer.

Harries, Dennis; Langenhorst, Falko (2013): The nanoscale mineralogy of Fe,Ni sulfides in pristine and metamorphosed CM and CM/CI-like chondrites: Tapping a petrogenetic record. In *Meteorit Planet Sci* 48 (5), pp. 879–903. DOI: 10.1111/maps.12089.

Hidalgo, Tania; Verrall, Michael; Beinlich, Andreas; Kuhar, Laura; Putnis, Andrew (2020): Replacement reactions of copper sulphides at moderate temperature in acidic solutions. In *Ore Geology Reviews* 123, p. 103569. DOI: 10.1016/j.oregeorev.2020.103569.

Janecky, D. R.; Seyfried, W. E. (1986): Hydrothermal serpentinization of peridotite within the oceanic crust: Experimental investigations of mineralogy and major element chemistry. In *Geochimica et Cosmochimica Acta* 50 (7), pp. 1357–1378. DOI: 10.1016/0016-7037(86)90311-X.

Kaneda, H.; Takenouchi, S.; Shoji, T. (1986): Stability of pentlandite in the Fe-Ni-Co-S system. In *Mineral. Deposita* 21 (3), pp. 169–180.

Klein, F.; Bach, W. (2009): Fe-Ni-Co-O-S Phase Relations in Peridotite-Seawater Interactions. In *Journal of Petrology* 50 (1), pp. 37–59. DOI: 10.1093/petrology/egn071.

Lollar, B. Sherwood; Lacrampe-Couloume, G.; Voglesonger, K.; Onstott, T. C.; Pratt, L. M.; Slater, G. F. (2008): Isotopic signatures of CH₄ and higher hydrocarbon gases from Precambrian Shield sites: A model for abiogenic polymerization of hydrocarbons. In *Geochimica et Cosmochimica Acta* 72 (19), pp. 4778–4795. DOI: 10.1016/j.gca.2008.07.004.

Lorand, J. aP (1989a): Abundance and distribution of CuFeNi sulfides, sulfur, copper and platinum-group elements in orogenic-type spinel lherzolite massifs of Ariège (Northeastern Pyrenees, France). In *Earth and Planetary Science Letters* 93 (1), pp. 50–64.

Lorand, J. P. (1985): The behaviour of the upper mantle sulfide component during the incipient alteration of “Alpine”-type peridotites as illustrated by the Beni Bousera (northern Morocco) and Ronda (southern Spain) ultramafic bodies. In *Tschermaks mineralogische und petrographische Mitteilungen* 34 (3-4), pp. 183–209.

Lorand, J. P. (1989b): Mineralogy and chemistry of Cu-Fe-Ni sulfides in orogenic-type spinel peridotite bodies from Ariege (Northeastern Pyrenees, France). In *Contributions to Mineralogy and Petrology* 103 (3), pp. 335–345.

Meyer-Dombard, D'Arcy R.; Woycheese, Kristin M.; Yargıcıoğlu, Erin N.; Cardace, Dawn; Shock, Everett L.; Güleçal-Pektaş, Yasemin; Temel, Mustafa (2015): High pH microbial ecosystems in a newly discovered, ephemeral, serpentinizing fluid seep at Yanartaş (Chimera), Turkey. In *Frontiers in microbiology* 5, p. 723.

Murphy, E. L.; Good, R. H. (1956): Thermionic Emission, Field Emission, and the Transition Region. In *Phys. Rev.* 102 (6), pp. 1464–1473. DOI: 10.1103/PhysRev.102.1464.

Nickel, Ernest Henry (1959): The occurrence of native nickel-iron in the serpentine rock of the Eastern Townships of Quebec Province. In *The Canadian Mineralogist* 6 (3), pp. 307–319.

Reed, Stephen Jarvis Brent (2005): Electron microprobe analysis and scanning electron microscopy in geology: Cambridge university press.

Rohne, Roxana (2019): Sulfur Geochemistry of Serpentinites from the Chimaera Site (Turkey). Master thesis. Freie Universität Berlin, Berlin. Institut für Geologische Wissenschaften.

Schwarzenbach, Esther M.; Früh-Green, Gretchen L.; Bernasconi, Stefano M.; Alt, Jeffrey C.; Shanks III, Wayne C.; Gaggero, Laura; Crispini, Laura (2012): Sulfur geochemistry of peridotite-hosted hydrothermal systems: comparing the Ligurian ophiolites with oceanic serpentinites. In *Geochimica et Cosmochimica Acta* 91, pp. 283–305.

Schwarzenbach, Esther M.; Gazel, Esteban; Caddick, Mark J. (2014): Hydrothermal processes in partially serpentinized peridotites from Costa Rica: evidence from native copper and complex sulfide assemblages. In *Contrib Mineral Petrol* 168 (5). DOI: 10.1007/s00410-014-1079-2.

Snow, Jonathan E.; Dick, Henry J.B. (1995): Pervasive magnesium loss by marine weathering of peridotite. In *Geochimica et Cosmochimica Acta* 59 (20), pp. 4219–4235. DOI: 10.1016/0016-7037(95)00239-V.

Stampfli, Gérard M.; Borel, Gilles D. (2004): The TRANSMED transects in space and time: constraints on the paleotectonic evolution of the Mediterranean domain. In : The TRANSMED Atlas. The Mediterranean region from crust to mantle: Springer, pp. 53–80.

Zwicker, J.; Birgel, D.; Bach, W.; Richoz, S.; Smrzka, D.; Grasemann, B. et al. (2018): Evidence for archaeal methanogenesis within veins at the onshore serpentinite-hosted Chimaera seeps, Turkey. In *Chemical Geology* 483, pp. 567–580. DOI: 10.1016/j.chemgeo.2018.03.027.

Appendix

EDS-maps (pp. 25-36)

Appendix figures 1-12 are all qualitative EDS-maps for the elements listed in each figure. Maps were created on a Zeiss Sigma VP Field Emission SEM, using Bruker Quantax Xflash 600mm² SSD EDS detectors and Bruker Esprit Version 2.1.2. Mapping time and image data can be found in the figures.

Green dots and numbers indicate EMPA-measurements, listed in Appendix table 1.

EMPA Measurement results (pp.37-44)

Appendix table 1 contains all point measurements taken by EMPA using wavelength-dispersive spectroscopy. As, Pb and Zn were measured, but no value had a standard deviation (SD) below 60%, which is why they were discarded altogether. If a measurement yielded an error considered too high, the element was marked as n.d. (not determined). Comments are the point where the measurement was taken, as marked in Appendix figures 1-12. Mineral names were classified with a self-written python 3.7.3-script, using the following constraints:

First, the measurements are loaded from the .txt files output by the EMP and sorted by grain. Only the elements Fe, Ni, S, Co, Cu are used, as the others have too high an error. If an element is below 0.06 wt%, it is removed. If the total is within 100 ± 2 wt%, the measurement is taken for the ternary plots (Figs. 2, 11) and classified. If it is within 100 ± 4 wt%, the measurement is classified, but the classification is bracketed manually in the final table. All measurements are then recalculated into at%, after which the classification algorithm is called upon. It works as follows:

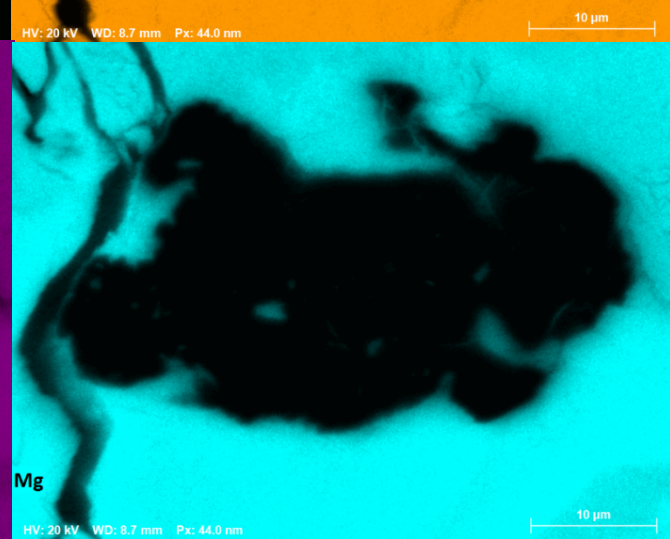
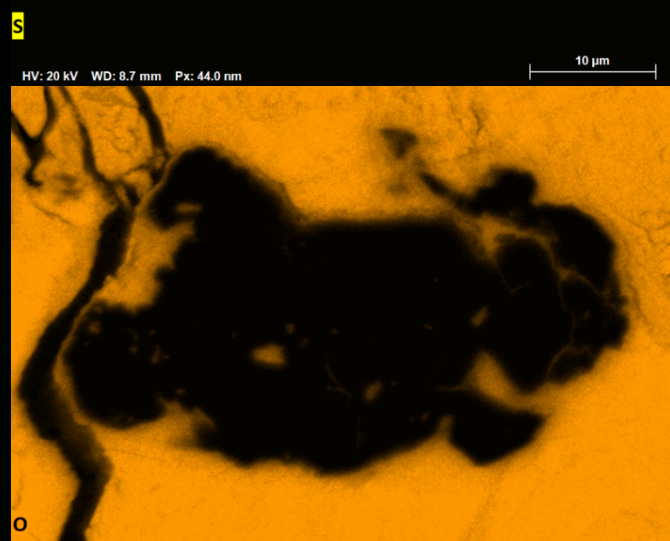
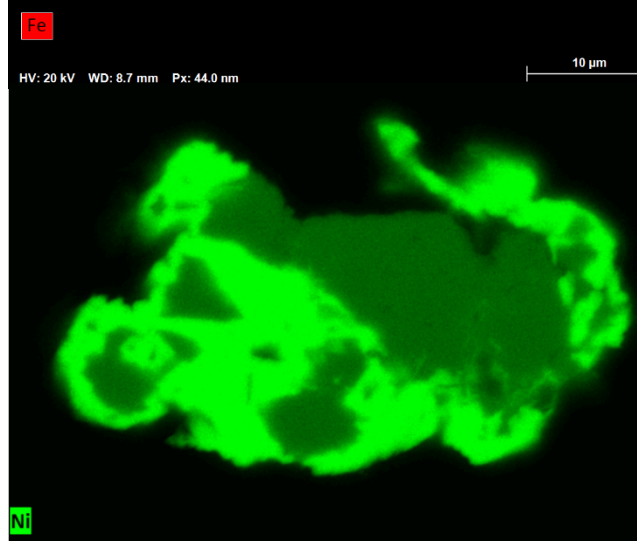
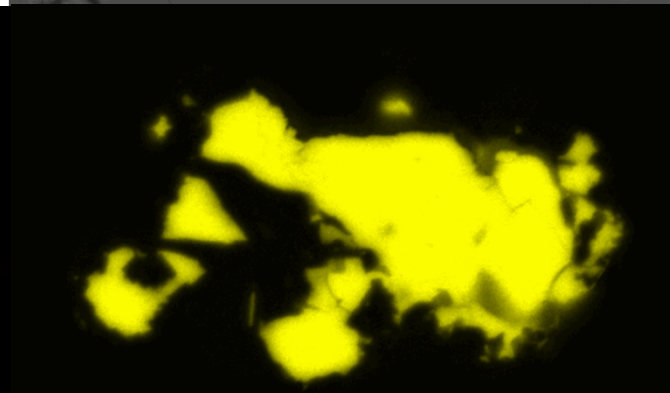
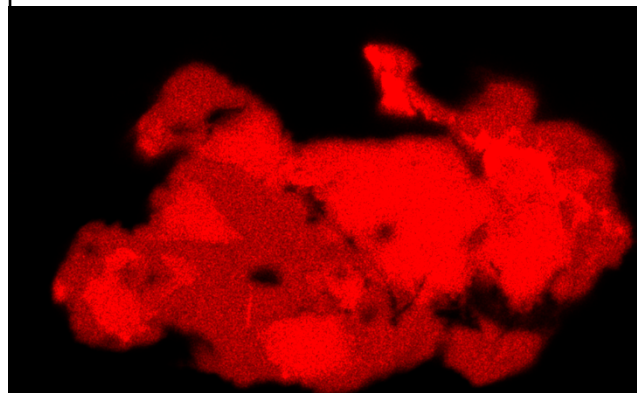
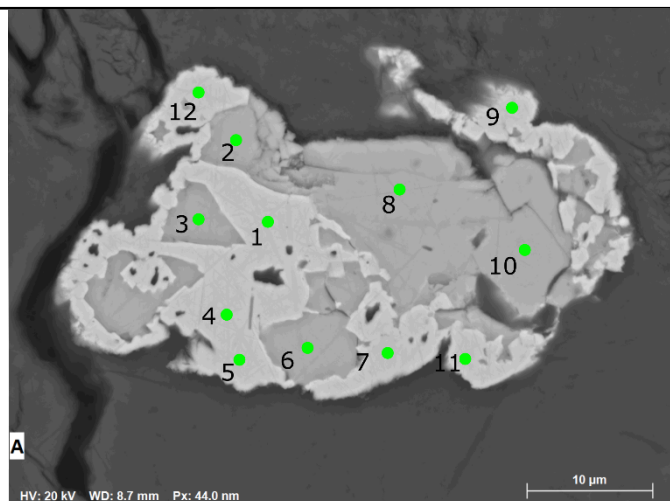
If the S content is above 25 at%, sulphides are checked in the order: millerite, heazlewoodite, godlevskite, pentlandite, samaniite, sugakiite, bornite, chalcocite. Compositions are as in Table 1 (Introduction). If none of them fit, the measurement is simply classified as "sulphide". This only happens for 2 measurements in CS26_R14, both with about 60 wt% Cu and very likely to be mixed measurements of possible native Cu and surrounding Cu-rich sulphides. Both these measurements yielded totals above 102 wt%.

When S is below 25 at% and high enough totals are still yielded in the measurement, it is most likely awaruite in this thesis, which is prone to mixed measurements due to its small size in the samples. If the atomic Fe/Ni ratio is within 1/3-1/2, the measurement is classified as awaruite. The number 25 as threshold for wt% S lead to two measurements that are most likely mixed measurements of both pentlandite and awaruite to be classified as either one, they were changed manually to "mixed". The number could also be lowered, but since all classifications except the two were in order, judging from the ternary plots, this was not done.

Appendix figure 1:
qualitative EDS-mapping of
Fe, S, Ni, O, Si, Mg
Mapping time: 1h

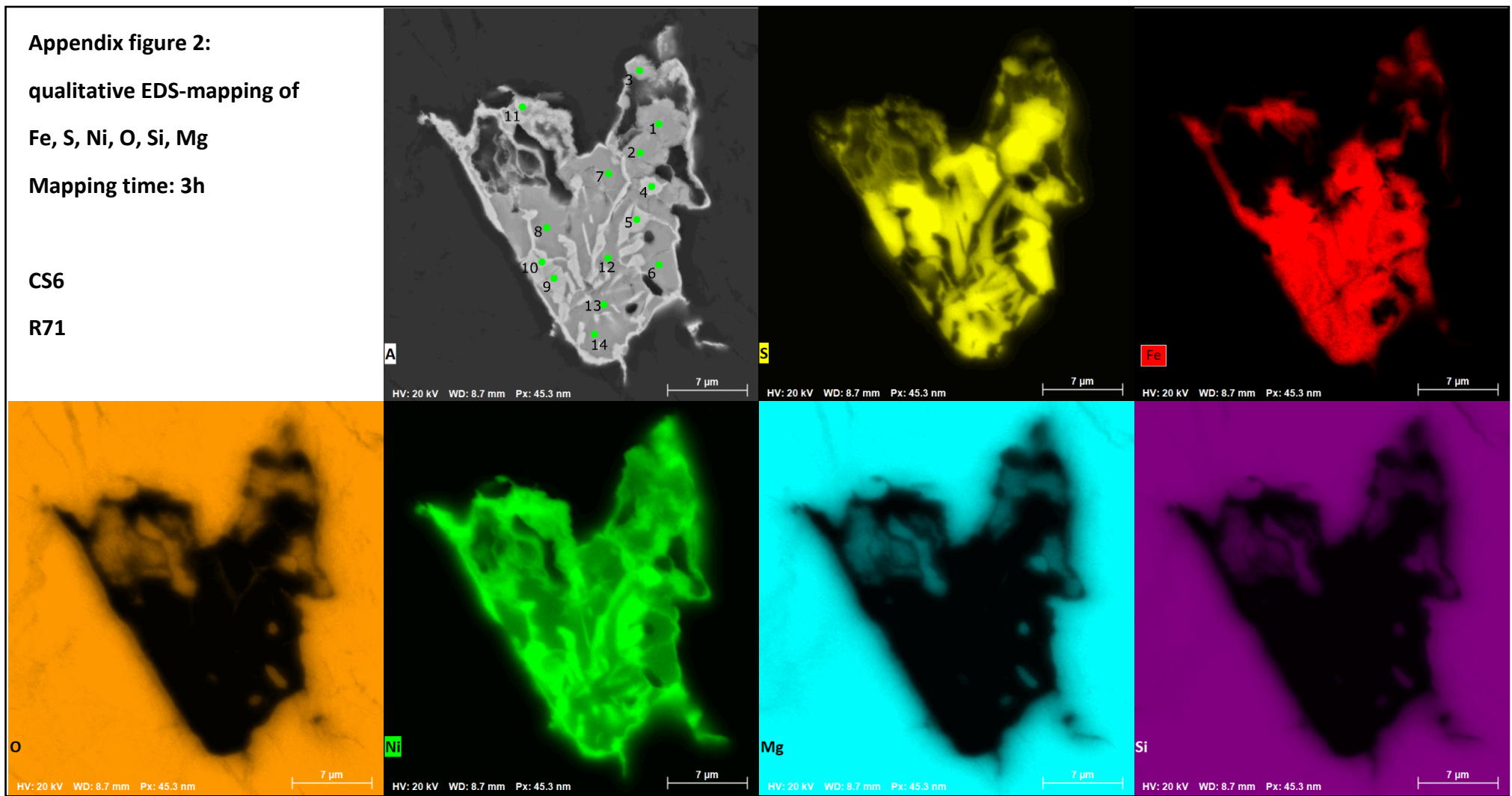
CS6

R61

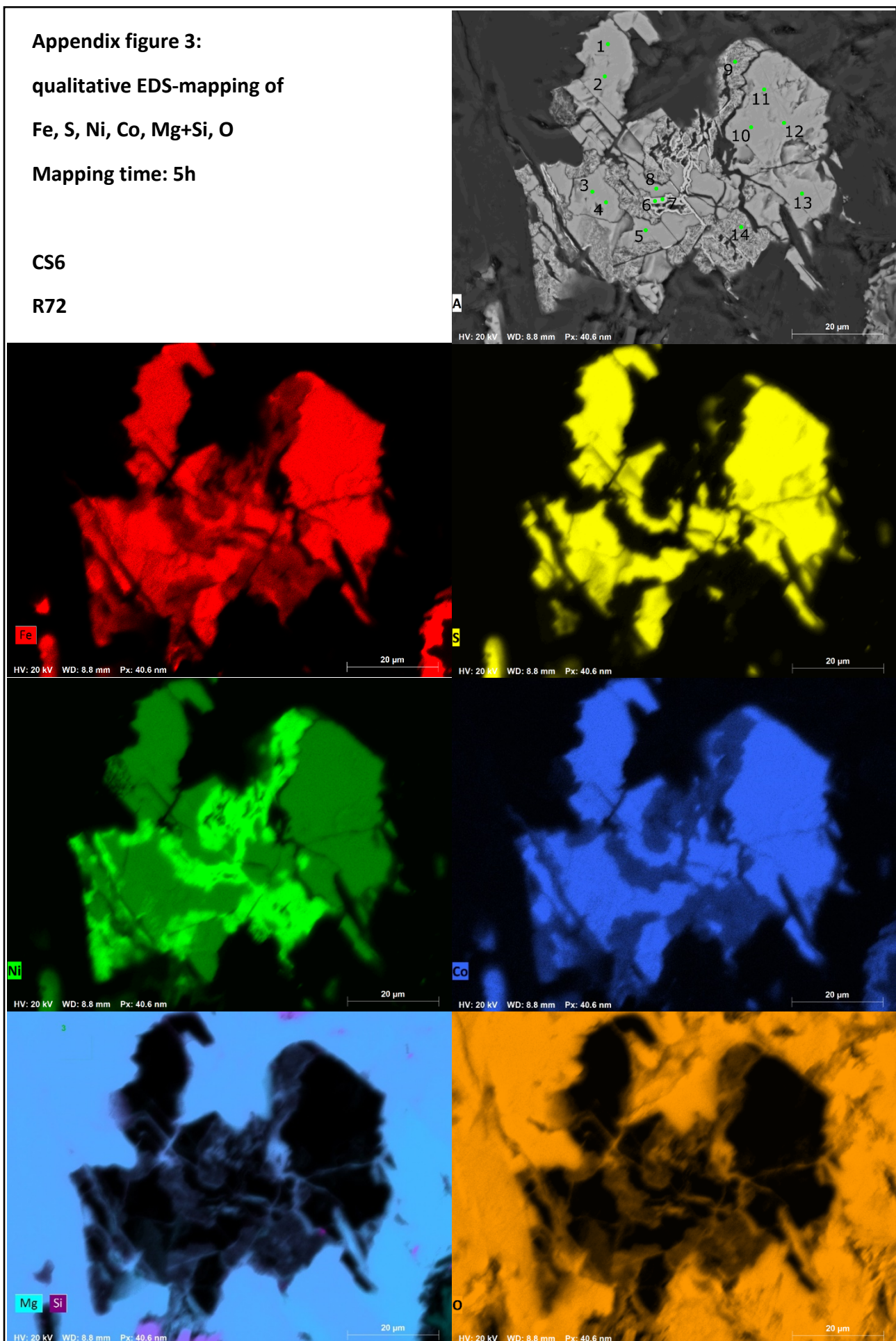


Appendix figure 2:
qualitative EDS-mapping of
Fe, S, Ni, O, Si, Mg
Mapping time: 3h

CS6
R71



Appendix figure 3:
qualitative EDS-mapping of
Fe, S, Ni, Co, Mg+Si, O
Mapping time: 5h



Appendix figure 4:

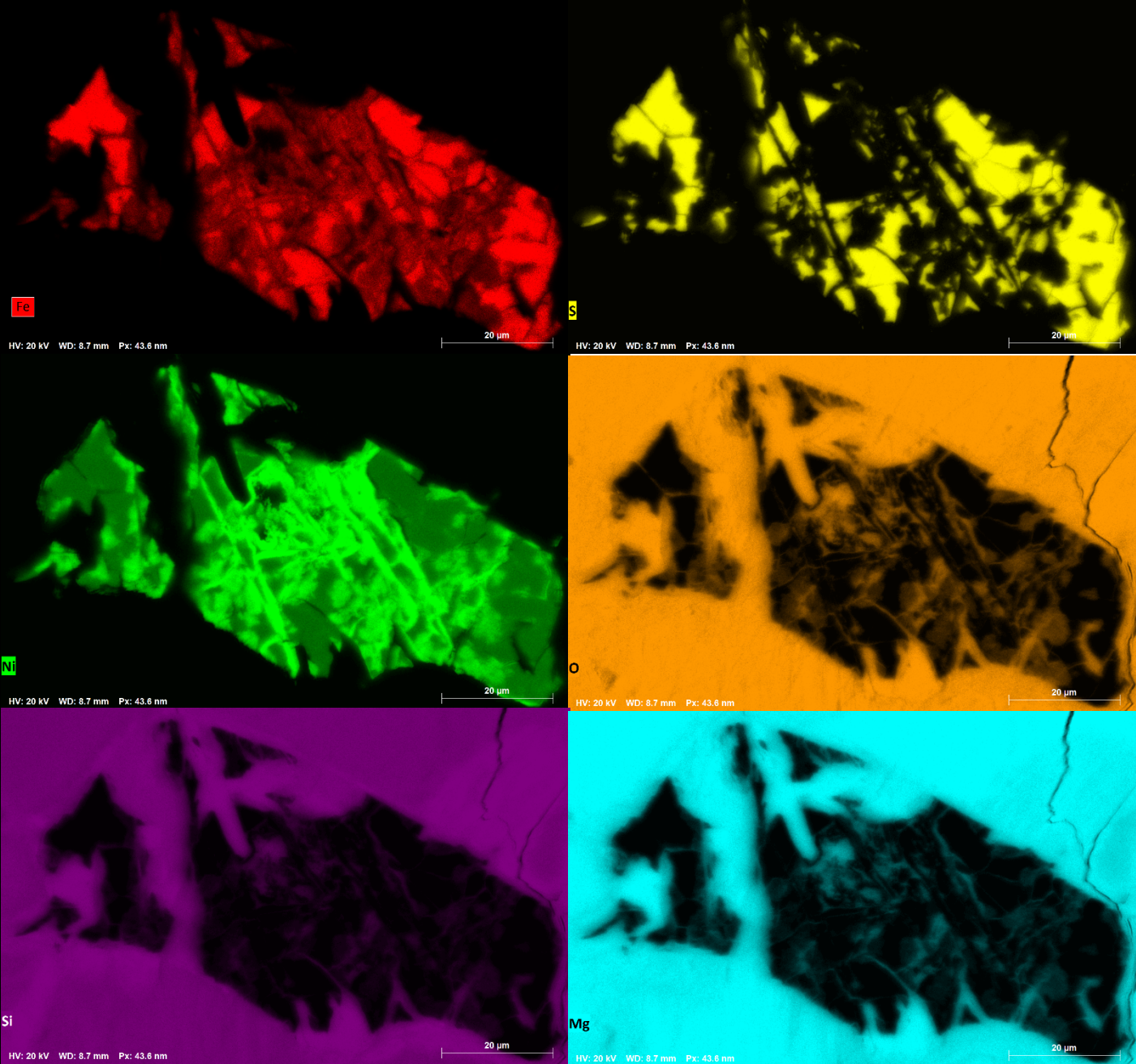
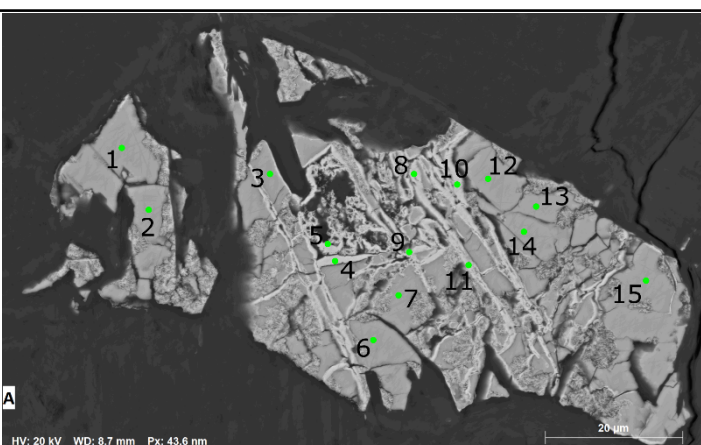
qualitative EDS-mapping of

Fe, S, Ni, O, Si, Mg

Mapping time: 3h

CS6

R73

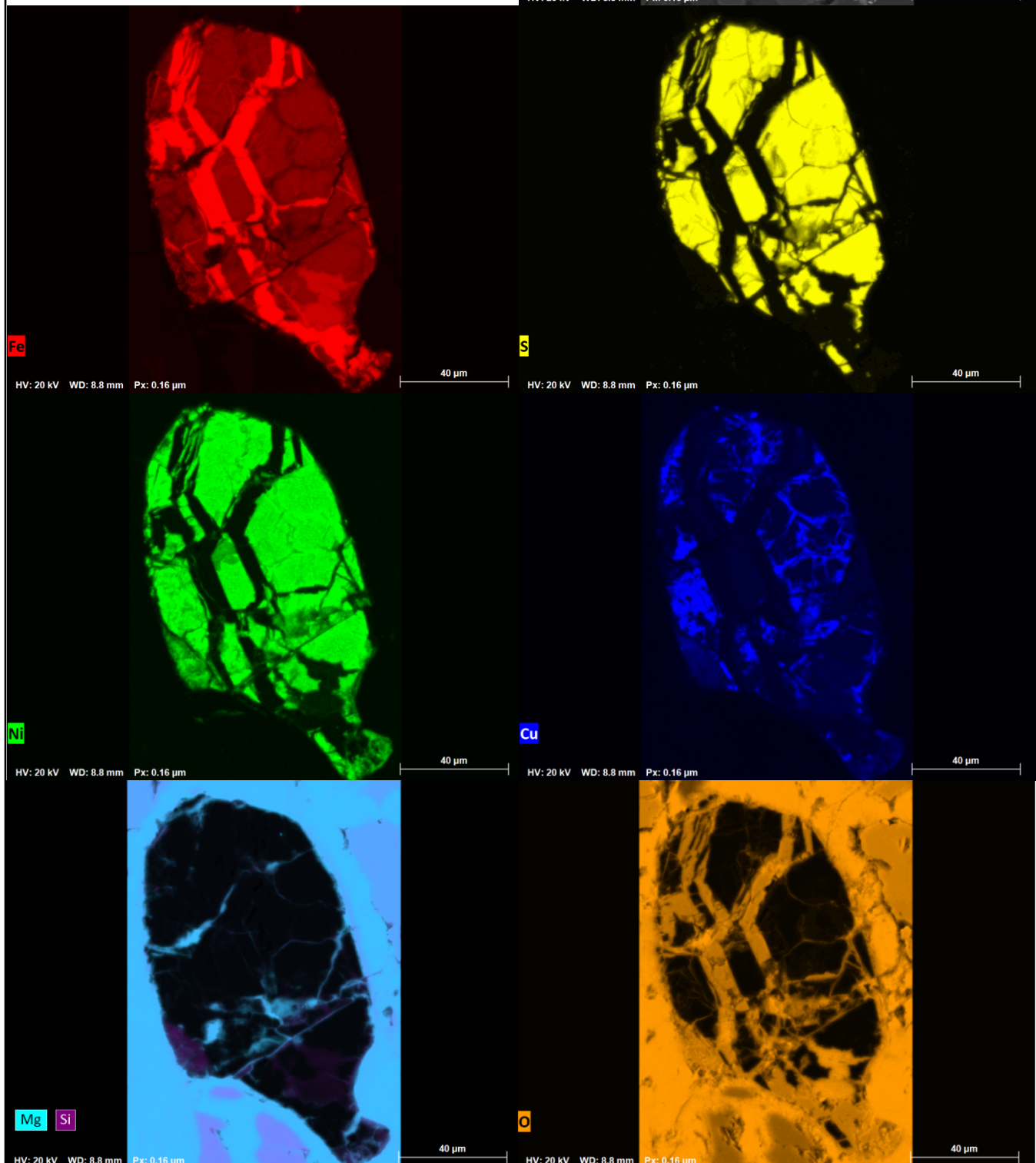
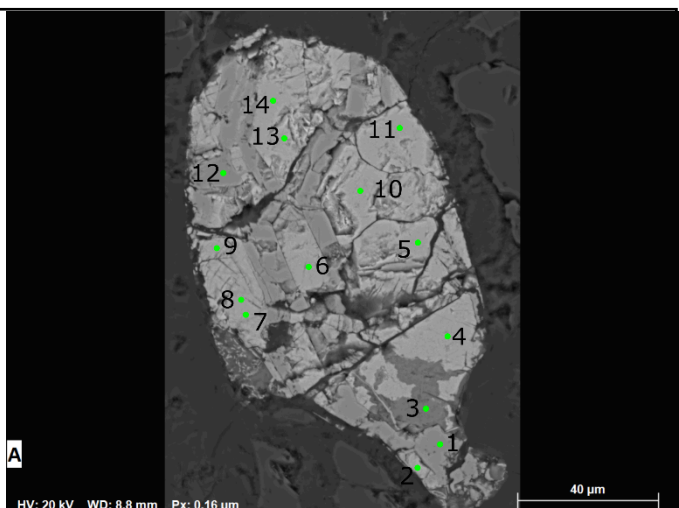


Appendix figure 5:
qualitative EDS-mapping of
Fe, S, Ni, Cu, Mg+Si, O

Mapping time: 3h

CS10

R14

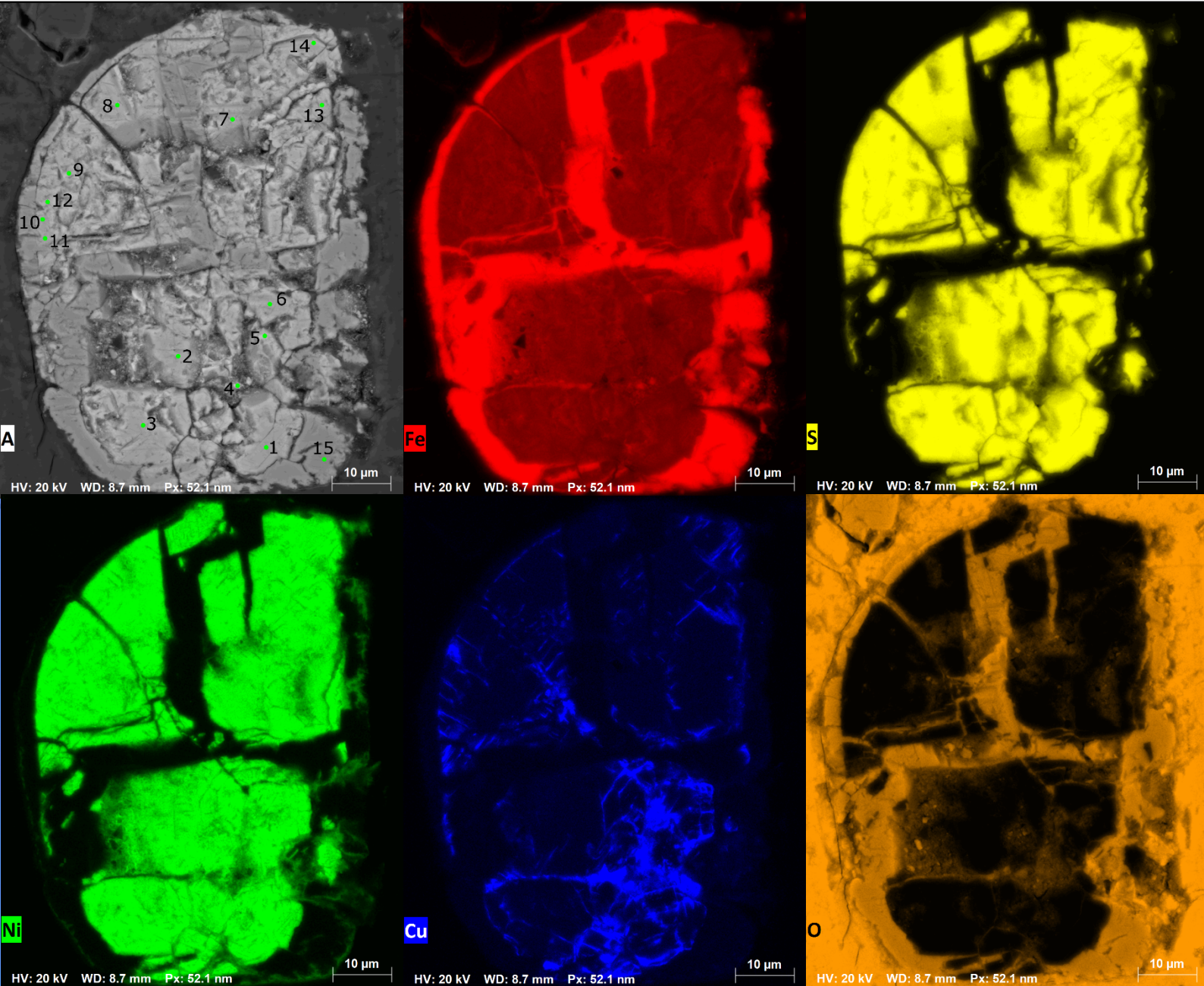


Appendix figure 6:
qualitative EDS-mapping of
Fe, S, Mg+Si, Ni, Cu, O

Mapping time: 5h

CS10

R32



Appendix figure 7:

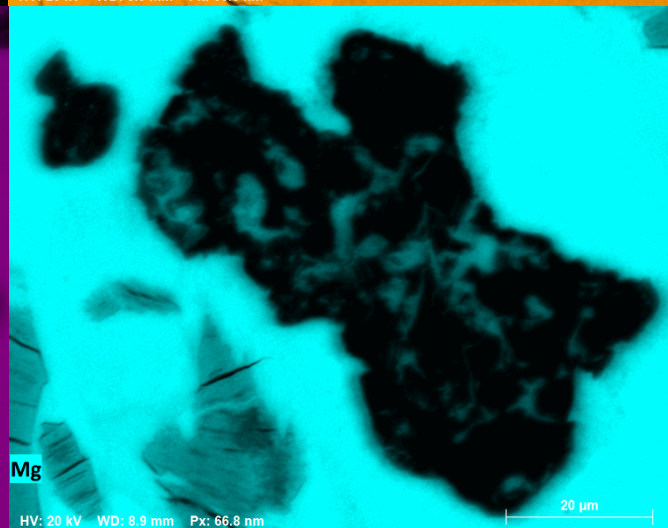
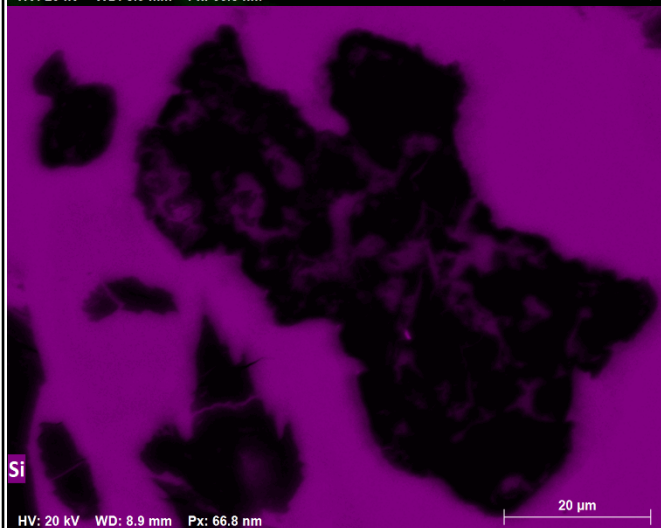
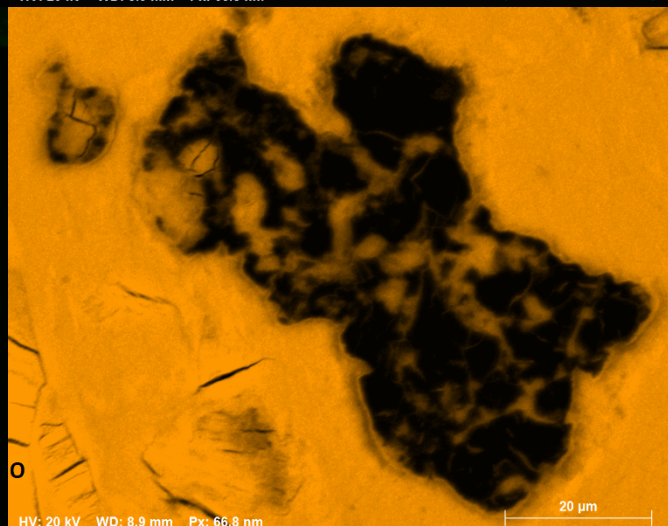
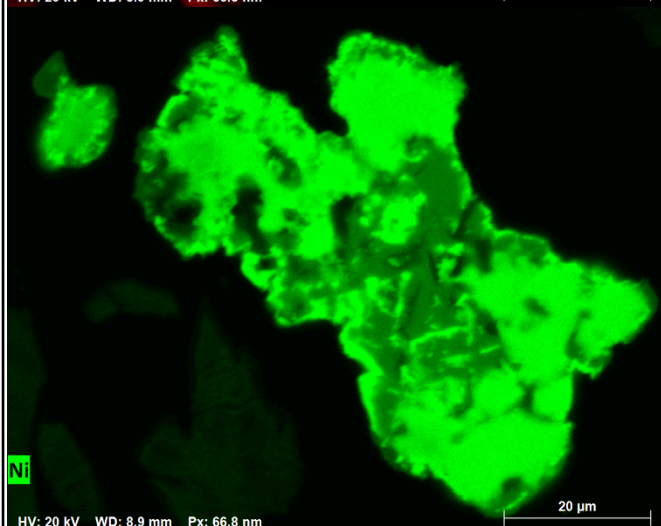
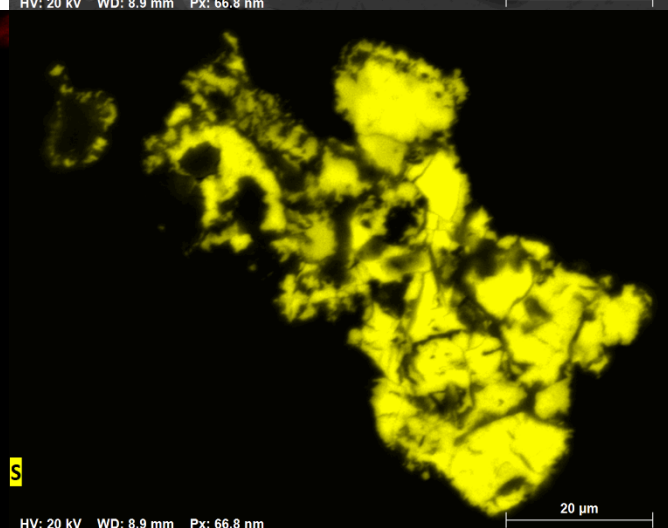
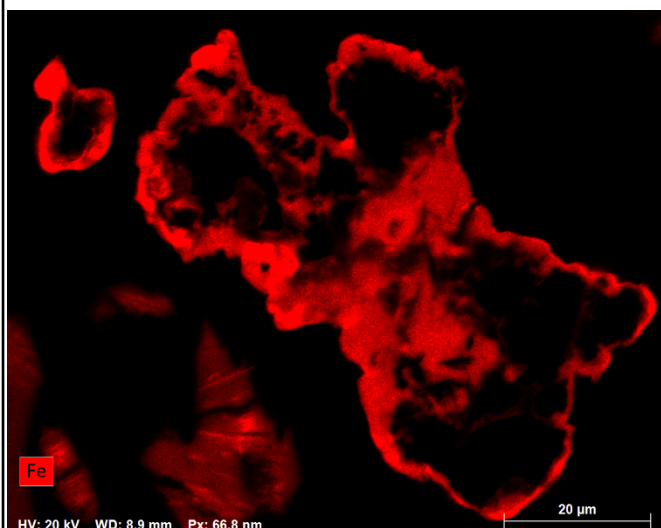
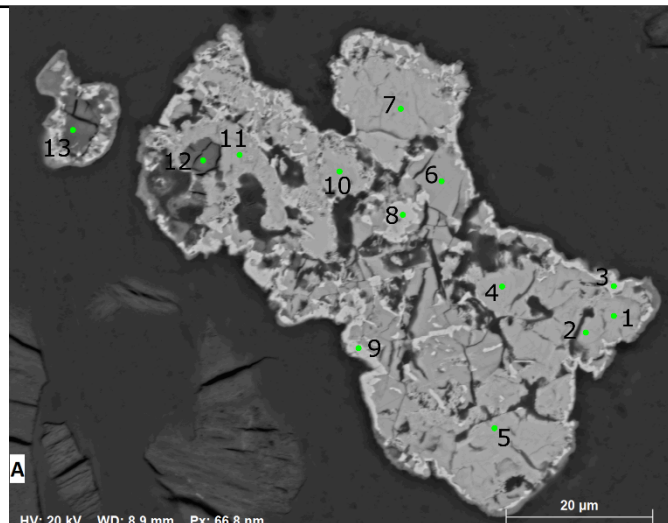
qualitative EDS-mapping of

Fe, S, Ni, O, Si, Mg

Mapping time: 3h

CS22

R13_1



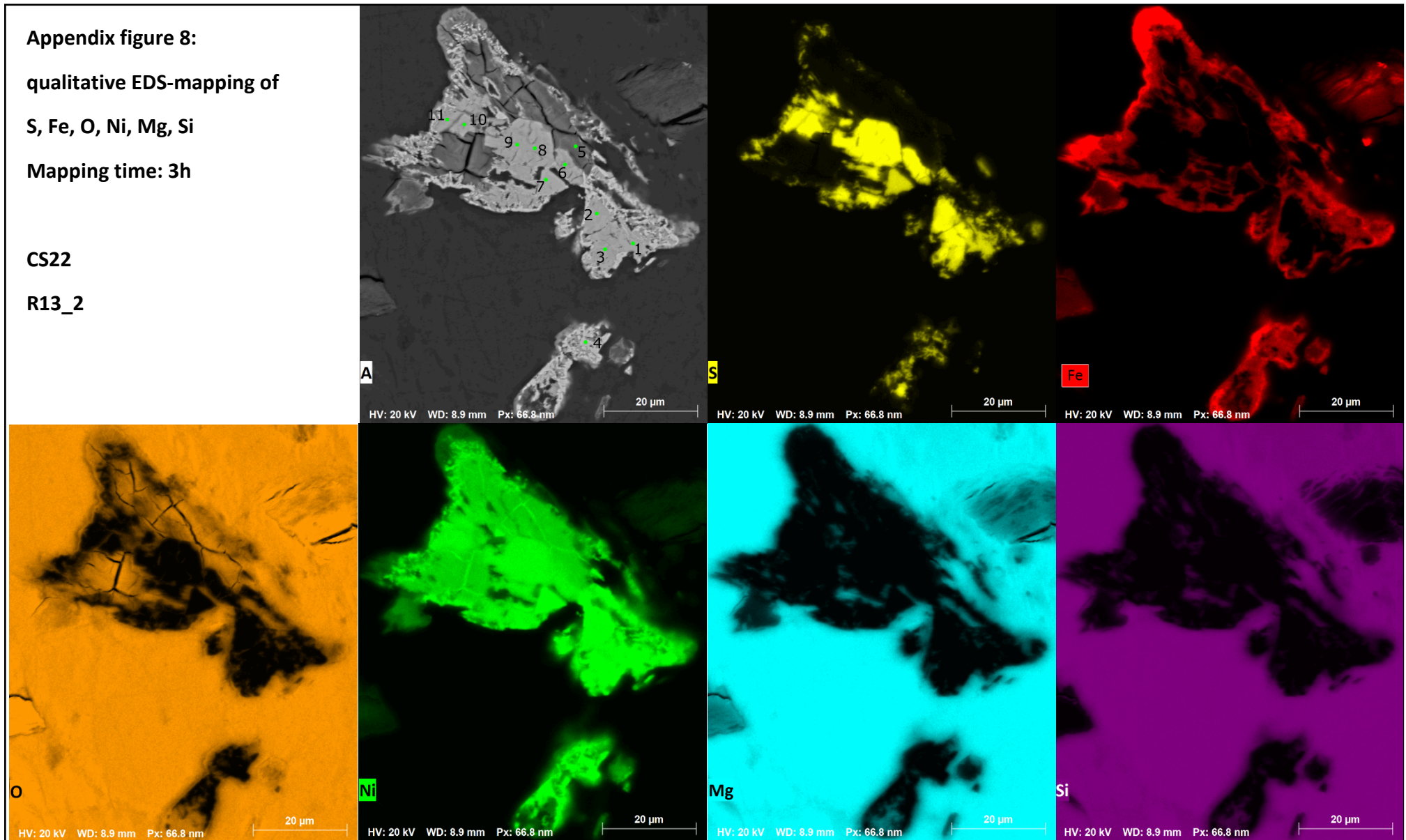
Appendix figure 8:
qualitative EDS-mapping of

S, Fe, O, Ni, Mg, Si

Mapping time: 3h

CS22

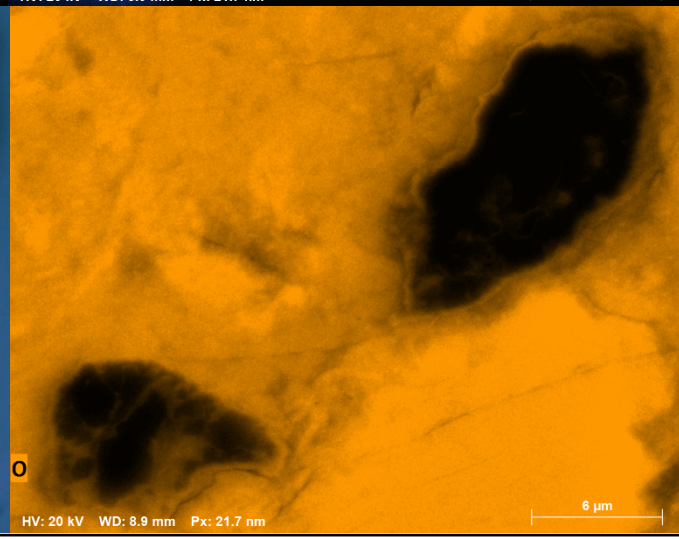
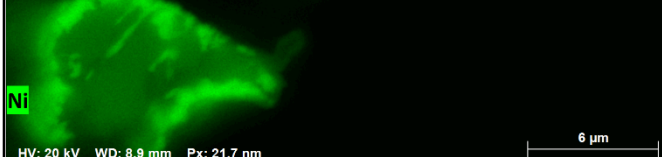
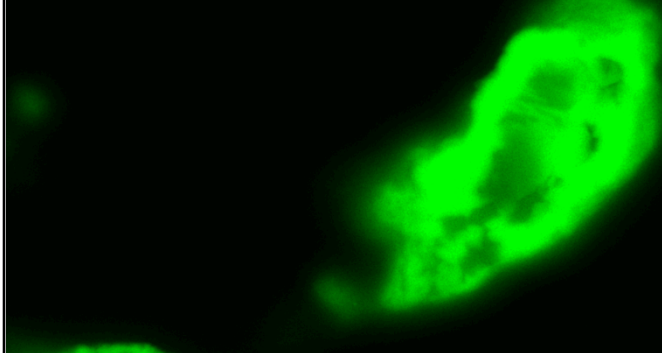
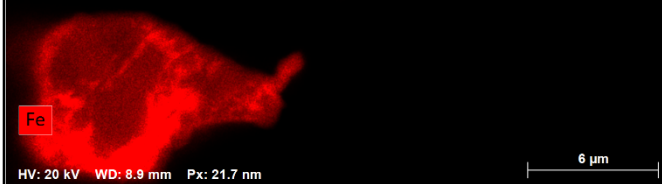
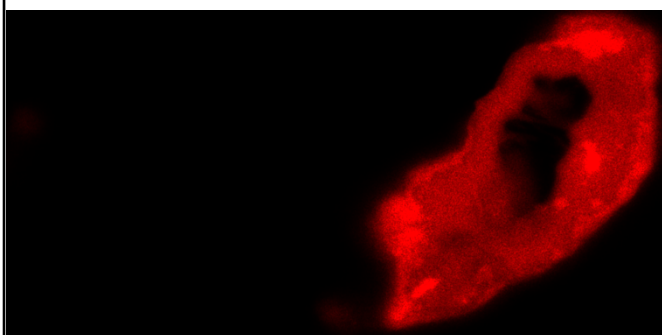
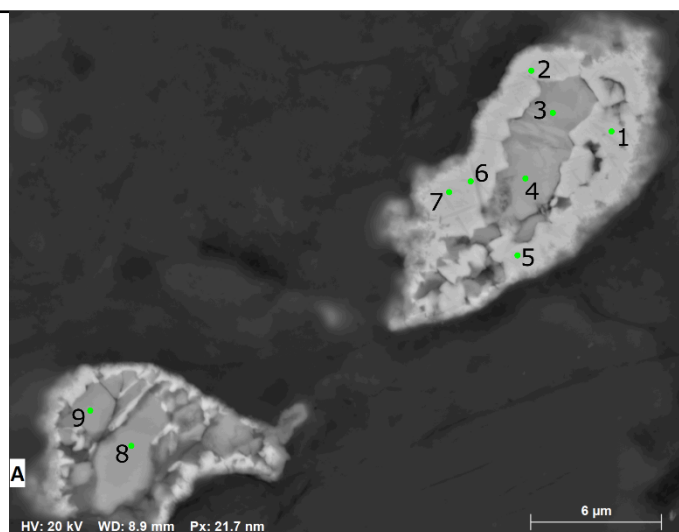
R13_2



Appendix figure 9:
qualitative EDS-mapping of
Fe, S, Ni, Co, Mg+Si, O
Mapping time: 3h

CS22

R21



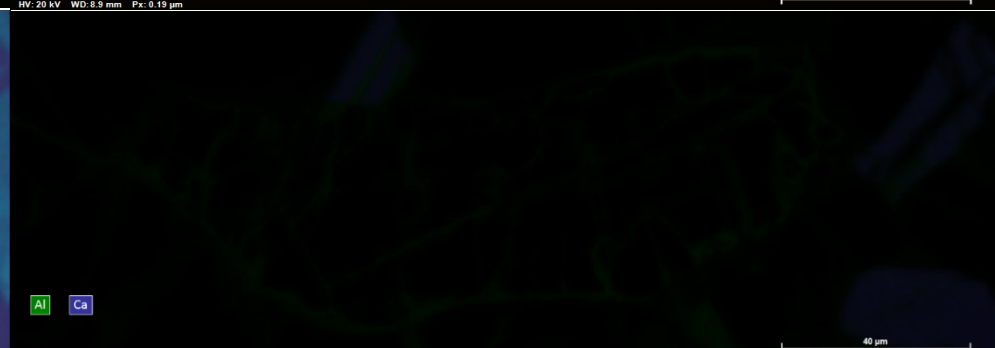
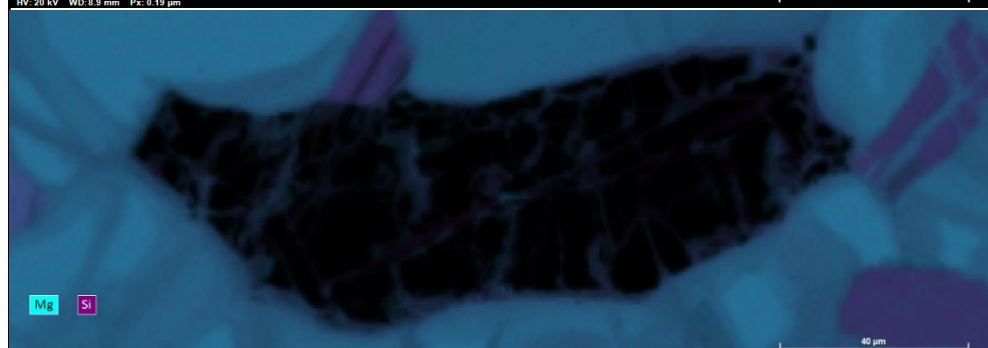
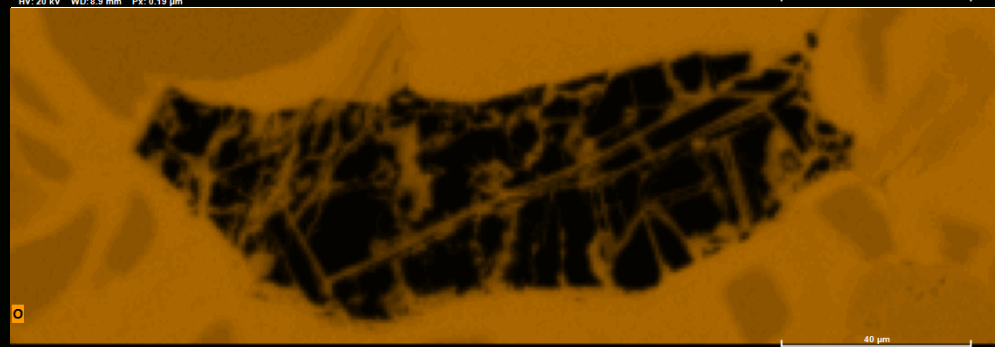
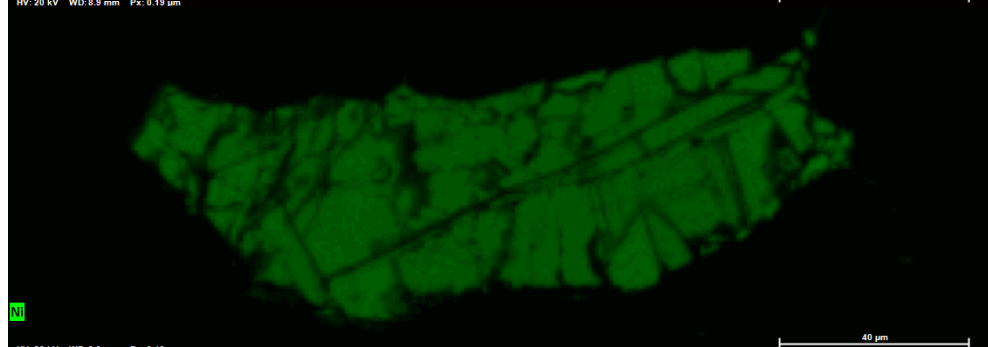
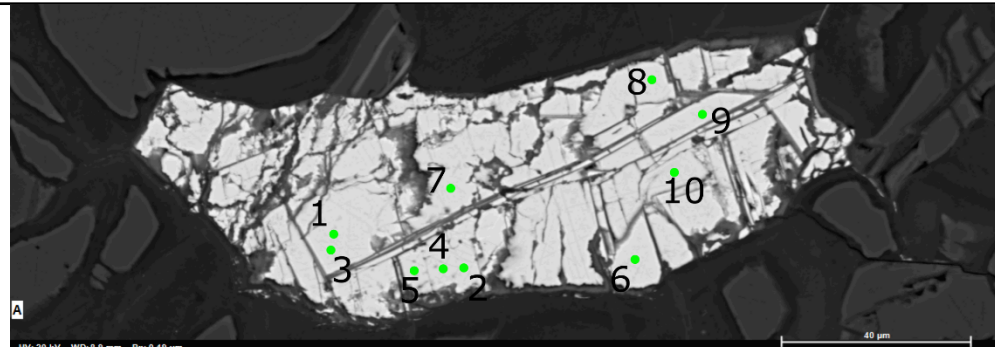
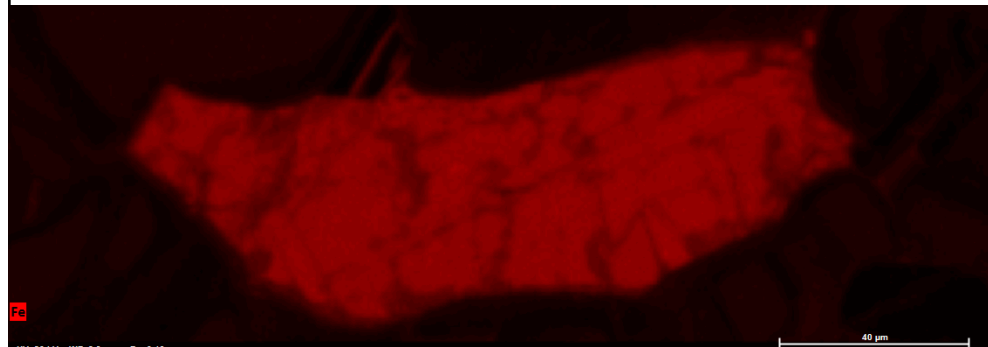
Appendix figure 10:

qualitative EDS-mapping of Fe, S, Ni, O, Mg+Si, Ca+Al

Mapping time: 30 min

CS 26

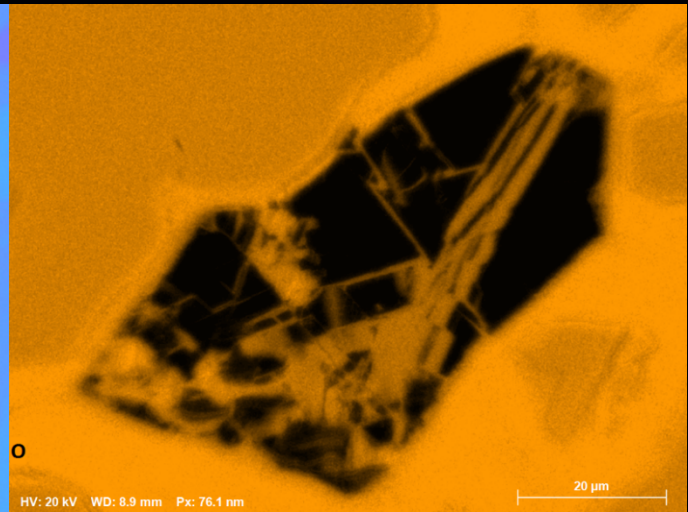
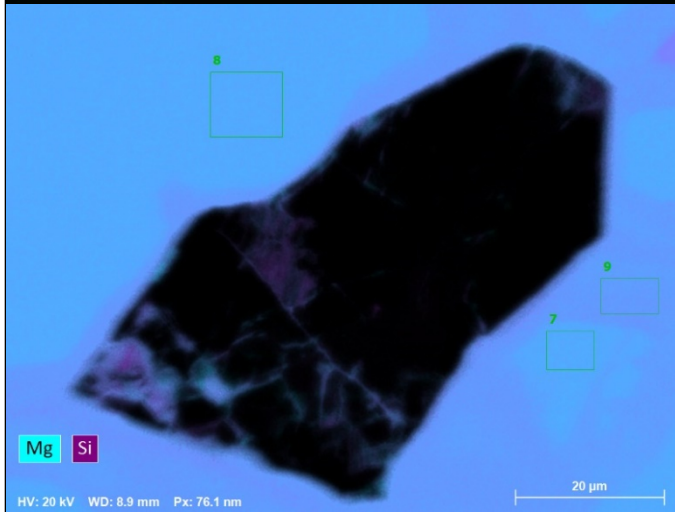
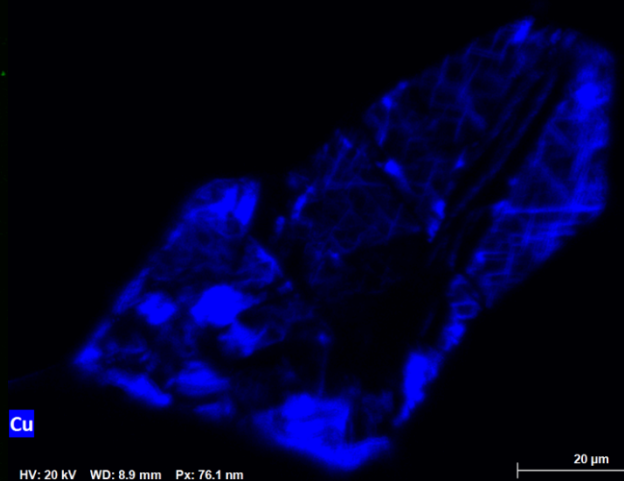
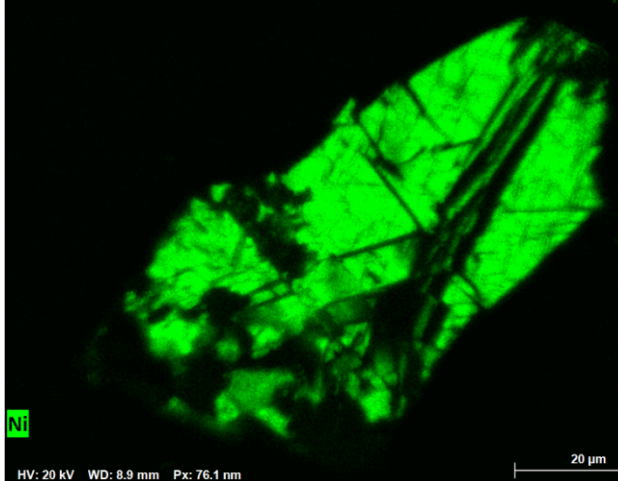
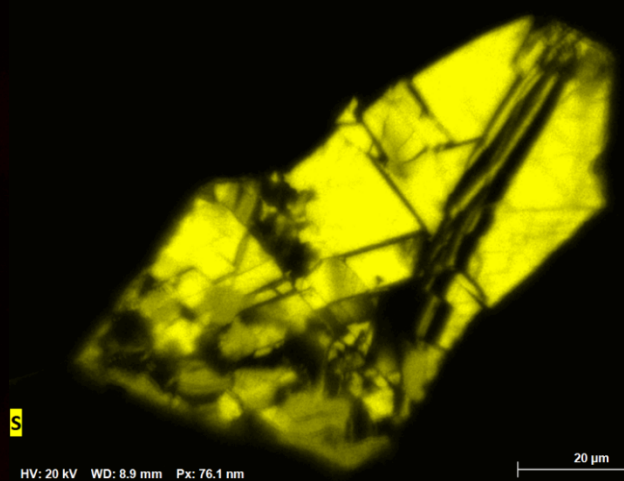
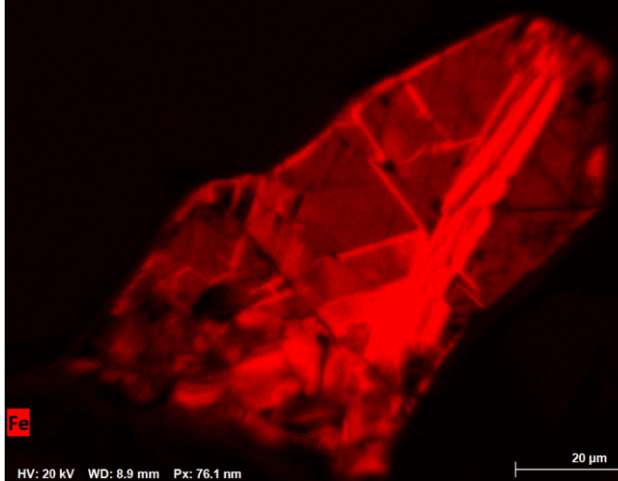
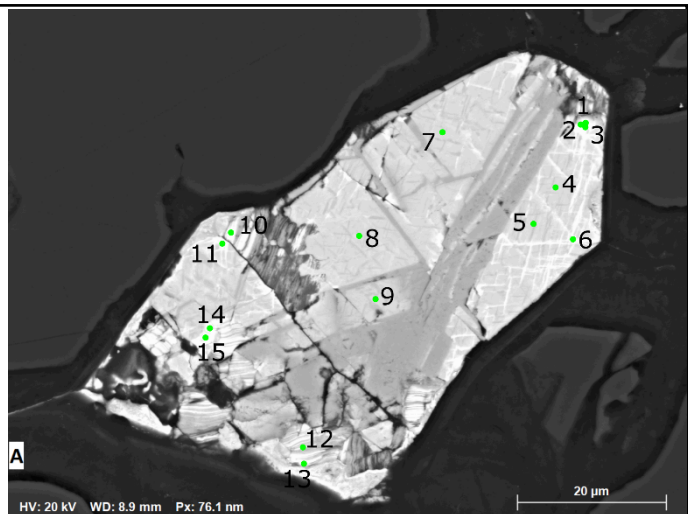
R10



Appendix figure 11:
qualitative EDS-mapping of
Fe, S, Ni, Cu, Si+Mg, O
Mapping time: 1h

CS26

R14

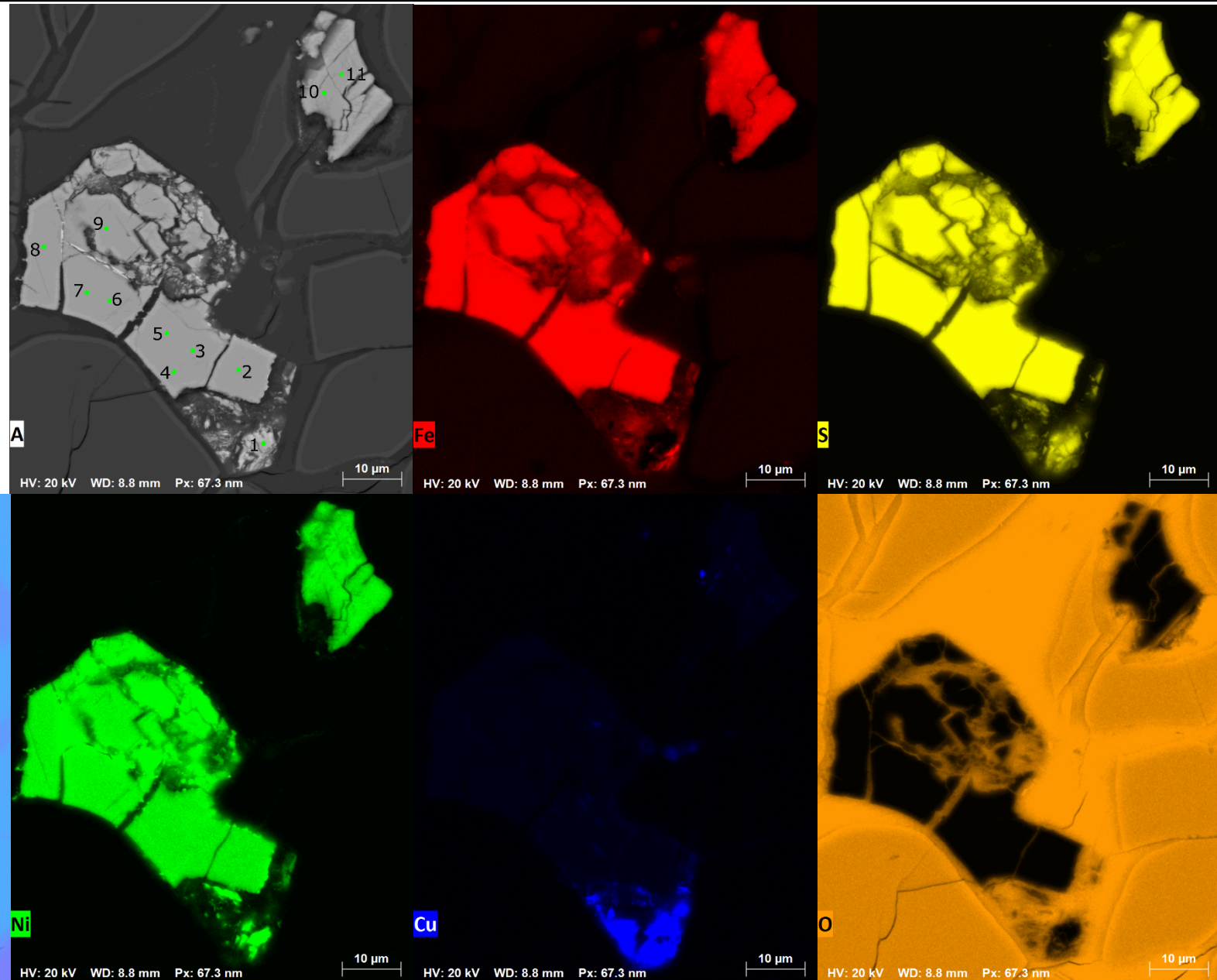
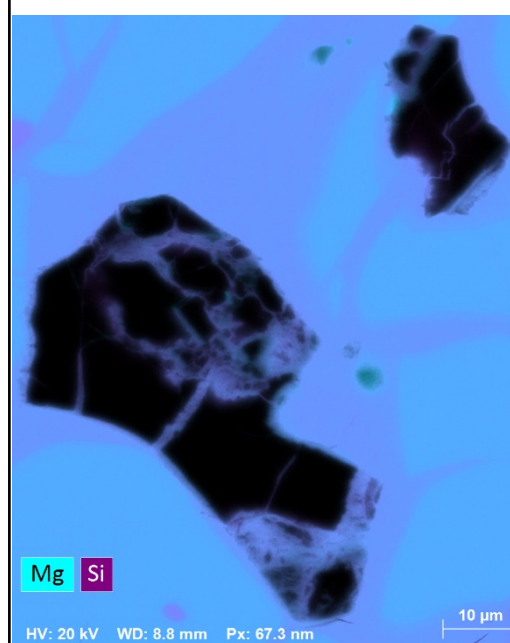


Appendix figure 12:
qualitative EDS-mapping of
Fe, S, Mg+Si, Ni, Cu, O

Mapping time: 3h

CS26

R16



No.	Comment	Ni	\pm [wt%]	S	\pm [wt%]	Fe	\pm [wt%]	Cu	\pm [wt%]	Co	SD[wt%]	total	\pm [wt%]	mineral
1	CS26_R10_1	26.08	0.14	33.71	0.21	38.33	0.16	1.14	0.05	0.47	0.03	99.72	0.60	pentlandite
2	CS26_R10_2	27.02	0.15	33.26	0.21	36.08	0.16	2.58	0.06	0.55	0.03	99.48	0.61	pentlandite
3	CS26_R10_3	25.94	0.14	33.47	0.21	38.69	0.17	0.94	0.05	0.50	0.03	99.53	0.60	pentlandite
4	CS26_R10_4	20.98	0.13	33.40	0.21	34.14	0.16	11.14	0.11	0.48	0.03	100.13	0.63	pentlandite
5	CS26_R10_5	25.75	0.14	33.65	0.21	36.37	0.16	3.88	0.07	0.48	0.03	100.13	0.61	pentlandite
6	CS26_R10_6	27.05	0.15	33.80	0.21	37.58	0.17	n.d.	0.00	0.68	0.04	99.11	0.55	pentlandite
7	CS26_R10_7	25.15	0.14	33.68	0.21	39.23	0.17	0.99	0.05	0.62	0.03	99.67	0.60	pentlandite
8	CS26_R10_8	26.26	0.14	33.85	0.21	38.47	0.17	n.d.	0.00	0.64	0.04	99.23	0.55	pentlandite
9	CS26_R10_9	24.16	0.14	34.02	0.21	40.11	0.17	0.91	0.05	0.59	0.03	99.79	0.60	pentlandite
10	CS26_R10_10	24.33	0.14	34.15	0.21	40.35	0.17	n.d.	n.d.	0.55	0.03	99.55	0.55	pentlandite
11	CS26_R16_1	57.28	0.21	32.88	0.21	2.48	0.04	4.91	0.08	n.d.	n.d.	97.54	0.54	(millerite)
12	CS26_R16_2	26.03	0.14	33.90	0.21	37.92	0.16	n.d.	n.d.	0.64	0.04	98.49	0.55	pentlandite
13	CS26_R16_3	26.02	0.14	34.15	0.21	38.38	0.17	n.d.	n.d.	0.70	0.04	99.25	0.55	pentlandite
14	CS26_R16_4	26.22	0.14	34.11	0.21	38.04	0.16	n.d.	n.d.	0.67	0.04	99.03	0.55	pentlandite
15	CS26_R16_5	26.19	0.14	34.41	0.21	37.99	0.16	n.d.	n.d.	0.66	0.04	99.25	0.55	pentlandite
16	CS26_R16_6	27.11	0.15	33.82	0.21	37.60	0.17	n.d.	n.d.	0.52	0.03	99.06	0.55	pentlandite
17	CS26_R16_7	27.02	0.15	33.90	0.21	36.95	0.16	n.d.	n.d.	0.55	0.03	98.42	0.55	pentlandite
18	CS26_R16_8	26.79	0.14	34.13	0.21	37.11	0.16	n.d.	n.d.	0.52	0.03	98.55	0.55	pentlandite
19	CS26_R16_9	26.92	0.15	34.02	0.21	37.67	0.17	n.d.	n.d.	0.52	0.03	99.13	0.55	pentlandite
20	CS26_R16_10	29.33	0.15	32.83	0.20	32.91	0.15	n.d.	n.d.	0.30	0.03	95.36	0.54	n.d.

No.	Comment	Ni	\pm [wt%]	S	\pm [wt%]	Fe	\pm [wt%]	Cu	\pm [wt%]	Co	SD[wt%]	total	\pm [wt%]	mineral
21	CS26_R16_11	19.74	0.12	35.11	0.21	42.03	0.17	0.40	0.04	0.24	0.03	97.52	0.58	pentlandite
22	CS26_R14_1	0.40	0.03	18.26	0.16	4.46	0.06	67.52	0.24	0.08	0.02	90.73	0.51	n.d.
23	CS26_R14_2	0.48	0.03	19.99	0.16	3.40	0.05	74.38	0.25	n.d.	n.d.	98.25	0.50	chalcocite
24	CS26_R14_3	0.64	0.04	19.70	0.16	3.75	0.05	73.78	0.25	n.d.	n.d.	97.86	0.50	(chalcocite)
25	CS26_R14_4	24.76	0.14	32.93	0.20	31.03	0.15	10.20	0.10	0.56	0.03	99.48	0.63	pentlandite
26	CS26_R14_5	15.99	0.11	33.92	0.21	32.21	0.15	17.02	0.13	0.53	0.03	99.66	0.63	samaniite
27	CS26_R14_6	9.00	0.09	24.25	0.18	8.94	0.08	60.02	0.23	0.28	0.03	102.48	0.60	sulphide
28	CS26_R14_7	21.80	0.13	34.04	0.21	34.69	0.16	8.62	0.10	0.79	0.04	99.94	0.63	pentlandite
29	CS26_R14_8	26.29	0.14	33.56	0.21	36.06	0.16	2.79	0.06	0.55	0.03	99.26	0.61	pentlandite
30	CS26_R14_9	16.56	0.11	34.04	0.21	40.68	0.17	8.30	0.09	0.51	0.03	100.09	0.62	pentlandite
31	CS26_R14_10	4.43	0.06	19.68	0.16	8.05	0.07	63.69	0.24	0.41	0.03	96.26	0.56	(chalcocite)
32	CS26_R14_11	7.25	0.08	24.33	0.18	9.56	0.08	61.11	0.23	n.d.	n.d.	102.25	0.57	sulphide
33	CS26_R14_12	0.73	0.04	19.17	0.16	16.50	0.11	54.59	0.22	n.d.	n.d.	91.00	0.52	n.d.
34	CS26_R14_13	n.d.	n.d.	15.97	0.15	14.64	0.10	61.41	0.23	n.d.	n.d.	92.02	0.47	n.d.
35	CS26_R14_14	1.16	0.04	21.67	0.17	4.21	0.06	74.82	0.25	n.d.	n.d.	101.86	0.52	chalcocite
36	CS26_R14_15	2.23	0.05	21.02	0.17	4.36	0.06	72.10	0.25	n.d.	n.d.	99.71	0.52	chalcocite
37	CS10_R32_1	23.28	0.14	34.16	0.21	41.08	0.17	n.d.	n.d.	0.65	0.04	99.17	0.55	pentlandite
38	CS10_R32_2	26.27	0.14	34.22	0.21	39.51	0.17	n.d.	n.d.	0.59	0.03	100.58	0.55	pentlandite
39	CS10_R32_3	25.14	0.14	34.51	0.21	39.43	0.17	n.d.	n.d.	0.58	0.03	99.65	0.55	pentlandite
40	CS10_R32_4	2.75	0.05	4.18	0.07	59.15	0.20	0.99	0.05	0.19	0.03	67.25	0.40	n.d.

No.	Comment	Ni	\pm [wt%]	S	\pm [wt%]	Fe	\pm [wt%]	Cu	\pm [wt%]	Co	SD[wt%]	total	\pm [wt%]	mineral
41	CS10_R32_5	25.64	0.14	35.15	0.21	38.18	0.16	0.79	0.05	0.59	0.03	100.35	0.60	pentlandite
42	CS10_R32_6	24.23	0.14	33.94	0.21	39.00	0.17	1.21	0.05	0.69	0.04	99.06	0.60	pentlandite
43	CS10_R32_7	25.00	0.14	31.23	0.20	40.45	0.17	n.d.	n.d.	0.52	0.03	97.20	0.54	(pentlandite)
44	CS10_R32_8	26.65	0.14	33.71	0.21	37.46	0.16	n.d.	n.d.	0.68	0.03	98.80	0.55	pentlandite
45	CS10_R32_9	24.46	0.14	34.59	0.21	39.07	0.17	n.d.	n.d.	0.62	0.04	98.93	0.55	pentlandite
46	CS10_R32_10	26.01	0.14	34.18	0.21	36.42	0.16	3.19	0.07	0.59	0.03	100.38	0.61	pentlandite
47	CS10_R32_11	24.85	0.14	34.36	0.21	36.10	0.16	4.45	0.07	0.72	0.04	100.47	0.62	pentlandite
48	CS10_R32_12	25.84	0.14	33.83	0.21	36.59	0.16	1.77	0.06	0.56	0.03	98.60	0.60	pentlandite
49	CS10_R32_13	26.33	0.14	33.27	0.21	35.89	0.16	2.35	0.06	0.55	0.03	98.39	0.60	pentlandite
50	CS10_R32_14	25.48	0.14	34.05	0.21	38.78	0.17	n.d.	n.d.	0.54	0.03	98.85	0.55	pentlandite
51	CS10_R32_15	n.d.	n.d.	n.d.	n.d.	65.63	0.22	n.d.	n.d.	n.d.	n.d.	65.63	0.22	n.d.
52	CS10_R14_1	n.d.	n.d.	0.00	0.00	66.38	0.21	n.d.	n.d.	n.d.	n.d.	66.38	0.21	n.d.
53	CS10_R14_2	32.20	0.16	35.02	0.21	31.76	0.15	n.d.	n.d.	0.55	0.03	99.53	0.55	pentlandite
54	CS10_R14_3	1.65	0.04	n.d.	n.d.	49.22	0.19	0.95	0.04	n.d.	n.d.	51.82	0.27	n.d.
55	CS10_R14_4	22.59	0.13	34.98	0.21	41.23	0.17	n.d.	n.d.	0.45	0.03	99.25	0.55	pentlandite
56	CS10_R14_5	22.86	0.13	34.66	0.21	40.11	0.17	n.d.	n.d.	0.52	0.03	98.30	0.54	pentlandite
57	CS10_R14_6	24.35	0.14	34.84	0.21	40.22	0.17	n.d.	n.d.	0.51	0.03	99.92	0.55	pentlandite
58	CS10_R14_7	25.70	0.14	35.23	0.21	38.19	0.16	0.53	0.05	0.48	0.03	100.14	0.60	pentlandite
59	CS10_R14_8	24.62	0.14	35.11	0.21	38.22	0.16	0.90	0.05	0.54	0.03	99.39	0.59	pentlandite
60	CS10_R14_9	22.66	0.13	35.71	0.21	39.74	0.17	0.77	0.05	0.48	0.03	99.36	0.60	pentlandite

No.	Comment	Ni	\pm [wt%]	S	\pm [wt%]	Fe	\pm [wt%]	Cu	\pm [wt%]	Co	SD[wt%]	total	\pm [wt%]	mineral
61	CS10_R14_10	24.08	0.14	34.77	0.21	40.49	0.17	n.d.	n.d.	0.45	0.03	99.79	0.55	pentlandite
62	CS10_R14_11	25.25	0.14	34.61	0.21	39.41	0.17	n.d.	n.d.	0.43	0.03	99.70	0.55	pentlandite
63	CS10_R14_12	n.d.	n.d.	n.d.	n.d.	66.36	0.21	n.d.	n.d.	n.d.	n.d.	66.36	0.21	n.d.
64	CS10_R14_13	23.79	0.14	34.92	0.21	41.23	0.17	n.d.	n.d.	0.53	0.03	100.48	0.55	pentlandite
65	CS6_R61_1	73.55	0.23	n.d.	n.d.	24.96	0.12	n.d.	n.d.	0.91	0.04	99.45	0.39	awaruite
66	CS6_R61_2	36.65	0.17	28.49	0.19	31.91	0.15	n.d.	n.d.	1.68	0.05	98.72	0.55	mixed
67	CS6_R61_3	30.92	0.15	34.05	0.21	34.26	0.16	n.d.	n.d.	1.65	0.04	100.88	0.56	pentlandite
68	CS6_R61_4	72.85	0.23	n.d.	n.d.	24.63	0.12	n.d.	n.d.	0.90	0.04	98.64	0.39	awaruite
69	CS6_R61_5	73.51	0.23	n.d.	n.d.	24.37	0.12	n.d.	n.d.	0.45	0.03	98.33	0.39	awaruite
70	CS6_R61_6	29.47	0.15	34.05	0.21	34.87	0.16	n.d.	n.d.	1.54	0.04	99.93	0.56	pentlandite
71	CS6_R61_7	73.30	0.23	0.39	0.03	25.27	0.13	n.d.	n.d.	0.27	0.03	99.23	0.41	awaruite
72	CS6_R61_8	28.88	0.15	34.14	0.21	35.35	0.16	n.d.	n.d.	1.54	0.04	99.91	0.56	pentlandite
73	CS6_R61_9	73.24	0.23	n.d.	n.d.	25.37	0.13	n.d.	n.d.	n.d.	n.d.	98.92	0.35	awaruite
74	CS6_R61_10	29.05	0.15	33.85	0.21	35.35	0.16	n.d.	n.d.	1.38	0.04	99.63	0.56	pentlandite
75	CS6_R61_11	73.21	0.23	n.d.	n.d.	24.78	0.12	n.d.	n.d.	n.d.	n.d.	98.23	0.35	awaruite
76	CS6_R61_12	73.25	0.23	0.02	0.02	24.23	0.12	n.d.	n.d.	0.58	0.04	98.08	0.40	awaruite
77	CS6_R71_1	42.00	0.18	32.04	0.20	21.35	0.12	n.d.	n.d.	2.03	0.05	97.43	0.55	(pentlandite)
78	CS6_R71_2	43.16	0.18	30.84	0.20	20.90	0.12	n.d.	n.d.	2.09	0.05	97.00	0.55	(pentlandite)
79	CS6_R71_3	43.90	0.18	16.69	0.15	25.93	0.13	n.d.	n.d.	2.15	0.05	88.68	0.51	n.d.
80	CS6_R71_4	71.35	0.23	1.13	0.04	24.34	0.12	n.d.	n.d.	0.35	0.03	97.17	0.43	(awaruite)

No.	Comment	Ni	\pm [wt%]	S	\pm [wt%]	Fe	\pm [wt%]	Cu	\pm [wt%]	Co	SD[wt%]	total	\pm [wt%]	mineral
81	CS6_R71_5	68.97	0.22	3.06	0.07	25.38	0.13	n.d.	n.d.	0.55	0.03	97.96	0.45	(awaruite)
82	CS6_R71_6	33.05	0.16	33.08	0.21	29.95	0.14	n.d.	n.d.	1.84	0.05	97.91	0.55	(pentlandite)
83	CS6_R71_7	35.77	0.16	32.44	0.20	27.93	0.14	n.d.	n.d.	1.95	0.05	98.09	0.56	pentlandite
84	CS6_R71_8	31.93	0.16	33.22	0.21	31.62	0.15	n.d.	n.d.	1.79	0.05	98.56	0.56	pentlandite
85	CS6_R71_9	64.16	0.22	8.01	0.10	26.49	0.13	n.d.	n.d.	0.78	0.04	99.44	0.49	mixed
86	CS6_R71_10	69.30	0.22	2.17	0.06	25.96	0.13	n.d.	n.d.	0.40	0.03	97.83	0.44	(awaruite)
87	CS6_R71_11	53.68	0.20	11.01	0.12	24.37	0.13	n.d.	n.d.	4.85	0.07	93.91	0.51	n.d.
88	CS6_R71_12	37.41	0.17	27.07	0.19	29.74	0.14	n.d.	n.d.	1.70	0.04	95.91	0.54	n.d.
89	CS6_R71_13	39.93	0.18	27.15	0.19	28.45	0.14	n.d.	n.d.	1.55	0.04	97.08	0.55	(pentlandite)
90	CS6_R71_14	36.24	0.17	30.45	0.20	28.53	0.14	n.d.	n.d.	1.72	0.04	96.93	0.55	(pentlandite)
91	CS6_R72_1	28.56	0.15	33.66	0.21	31.84	0.15	n.d.	n.d.	3.64	0.06	97.70	0.57	(pentlandite)
92	CS6_R72_2	29.16	0.15	33.81	0.21	31.76	0.15	n.d.	n.d.	3.54	0.06	98.27	0.57	pentlandite
93	CS6_R72_3	28.57	0.15	33.87	0.21	33.75	0.16	n.d.	n.d.	3.34	0.06	99.52	0.57	pentlandite
94	CS6_R72_4	28.58	0.15	33.57	0.21	33.55	0.15	n.d.	n.d.	3.28	0.06	98.97	0.57	pentlandite
95	CS6_R72_5	29.21	0.15	33.49	0.21	32.89	0.15	n.d.	n.d.	3.31	0.06	98.89	0.57	pentlandite
96	CS6_R72_6	72.46	0.23	0.24	0.02	25.14	0.13	n.d.	n.d.	n.d.	n.d.	97.85	0.38	(awaruite)
97	CS6_R72_7	72.30	0.23	0.27	0.02	24.91	0.12	n.d.	n.d.	n.d.	n.d.	97.48	0.38	(awaruite)
98	CS6_R72_8	28.82	0.15	34.05	0.21	33.17	0.15	n.d.	n.d.	3.51	0.06	99.55	0.57	pentlandite
99	CS6_R72_9	48.23	0.19	1.04	0.04	19.28	0.11	n.d.	n.d.	n.d.	n.d.	68.55	0.34	n.d.
100	CS6_R72_10	28.19	0.15	33.52	0.21	33.34	0.15	n.d.	n.d.	3.71	0.06	98.76	0.57	pentlandite

No.	Comment	Ni	\pm [wt%]	S	\pm [wt%]	Fe	\pm [wt%]	Cu	\pm [wt%]	Co	SD[wt%]	total	\pm [wt%]	mineral
101	CS6_R72_11	28.16	0.15	34.13	0.21	33.47	0.15	n.d.	n.d.	3.60	0.06	99.36	0.57	pentlandite
102	CS6_R72_12	28.05	0.15	34.01	0.21	34.01	0.16	n.d.	n.d.	3.63	0.06	99.70	0.57	pentlandite
103	CS6_R72_13	27.88	0.15	34.15	0.21	33.94	0.16	n.d.	n.d.	3.55	0.06	99.51	0.57	pentlandite
104	CS6_R72_14	47.73	0.19	0.76	0.04	19.46	0.11	n.d.	n.d.	n.d.	n.d.	67.94	0.33	n.d.
105	CS6_R73_1	26.98	0.15	34.09	0.21	36.07	0.16	n.d.	n.d.	1.84	0.05	98.97	0.56	pentlandite
106	CS6_R73_2	29.17	0.15	33.36	0.21	33.69	0.15	n.d.	n.d.	2.04	0.05	98.26	0.56	pentlandite
107	CS6_R73_3	27.97	0.15	33.14	0.21	34.36	0.16	n.d.	n.d.	3.68	0.06	99.14	0.57	pentlandite
108	CS6_R73_4	72.49	0.23	0.41	0.03	25.47	0.13	n.d.	n.d.	n.d.	0.00	98.37	0.39	awaruite
109	CS6_R73_5	72.80	0.23	n.d.	n.d.	24.43	0.12	n.d.	n.d.	n.d.	0.00	97.23	0.36	(awaruite)
110	CS6_R73_6	26.94	0.15	33.33	0.21	34.94	0.16	n.d.	n.d.	3.62	0.06	98.83	0.57	pentlandite
111	CS6_R73_7	28.04	0.15	33.25	0.21	34.28	0.16	n.d.	n.d.	3.91	0.06	99.48	0.57	pentlandite
112	CS6_R73_8	72.15	0.23	1.89	0.05	24.82	0.13	n.d.	n.d.	0.32	0.03	99.18	0.44	awaruite
113	CS6_R73_9	67.48	0.22	3.91	0.07	24.23	0.12	n.d.	n.d.	0.53	0.03	96.15	0.46	(awaruite)
114	CS6_R73_10	72.65	0.23	0.19	0.02	24.80	0.12	n.d.	n.d.	n.d.	n.d.	97.64	0.38	(awaruite)
115	CS6_R73_11	69.34	0.22	2.61	0.06	23.10	0.12	n.d.	n.d.	n.d.	n.d.	95.05	0.40	n.d.
116	CS6_R73_12	26.64	0.14	34.13	0.21	36.71	0.16	n.d.	n.d.	2.64	0.05	100.11	0.57	pentlandite
117	CS6_R73_13	27.72	0.15	34.36	0.21	35.04	0.16	n.d.	n.d.	2.67	0.05	99.79	0.57	pentlandite
118	CS6_R73_14	28.36	0.15	34.36	0.21	34.84	0.16	n.d.	n.d.	2.73	0.05	100.29	0.57	pentlandite
119	CS6_R73_15	28.73	0.15	34.24	0.21	34.74	0.16	n.d.	n.d.	2.33	0.05	100.03	0.56	pentlandite
120	CS22_R21_1	71.43	0.23	0.56	0.03	23.72	0.12	n.d.	n.d.	0.45	0.03	96.16	0.42	(awaruite)

No.	Comment	Ni	\pm [wt%]	S	\pm [wt%]	Fe	\pm [wt%]	Cu	\pm [wt%]	Co	SD[wt%]	total	\pm [wt%]	mineral
121	CS22_R21_2	69.73	0.22	0.23	0.02	23.47	0.12	n.d.	n.d.	0.28	0.03	93.70	0.40	n.d.
122	CS22_R21_3	38.79	0.17	31.94	0.20	20.67	0.12	n.d.	n.d.	5.80	0.07	97.20	0.57	(pentlandite)
123	CS22_R21_4	52.41	0.20	29.81	0.20	11.64	0.09	n.d.	n.d.	3.49	0.06	97.35	0.55	(millerite)
124	CS22_R21_5	66.60	0.22	4.00	0.08	23.39	0.12	n.d.	n.d.	1.39	0.04	95.38	0.46	n.d.
125	CS22_R21_6	72.11	0.23	0.19	0.02	23.94	0.12	n.d.	n.d.	0.34	0.03	96.58	0.41	(awaruite)
126	CS22_R21_7	71.92	0.23	0.51	0.03	23.98	0.12	n.d.	n.d.	0.42	0.03	96.82	0.42	(awaruite)
127	CS22_R21_8	29.32	0.15	32.81	0.21	26.31	0.14	n.d.	n.d.	8.75	0.09	97.19	0.58	(pentlandite)
128	CS22_R21_9	29.35	0.15	31.92	0.20	25.73	0.14	n.d.	n.d.	8.86	0.09	95.85	0.58	n.d.
129	CS22_R13_1_1	64.79	0.22	33.88	0.21	1.27	0.03	n.d.	n.d.	n.d.	n.d.	99.94	0.47	millerite
130	CS22_R13_1_2	64.52	0.22	33.97	0.21	1.84	0.04	n.d.	n.d.	n.d.	n.d.	100.33	0.47	millerite
131	CS22_R13_1_3	69.54	0.22	2.91	0.07	23.06	0.12	n.d.	n.d.	1.50	0.04	97.00	0.45	(awaruite)
132	CS22_R13_1_4	65.37	0.22	33.71	0.21	1.41	0.04	n.d.	n.d.	n.d.	n.d.	100.49	0.47	millerite
133	CS22_R13_1_5	65.36	0.22	34.55	0.21	1.19	0.03	n.d.	n.d.	n.d.	n.d.	101.09	0.47	millerite
134	CS22_R13_1_6	30.13	0.15	34.09	0.21	27.16	0.14	n.d.	n.d.	7.81	0.08	99.19	0.58	pentlandite
135	CS22_R13_1_7	65.53	0.22	33.01	0.21	1.42	0.04	n.d.	n.d.	n.d.	n.d.	99.96	0.47	millerite
136	CS22_R13_1_8	58.25	0.20	0.19	0.02	20.94	0.12	n.d.	n.d.	1.05	0.04	80.43	0.38	n.d.
137	CS22_R13_1_9	69.05	0.22	0.63	0.03	23.91	0.12	n.d.	n.d.	0.59	0.04	94.17	0.41	n.d.
138	CS22_R13_1_10	65.33	0.22	33.11	0.21	1.94	0.04	n.d.	n.d.	n.d.	n.d.	100.38	0.47	millerite
139	CS22_R13_1_11	65.41	0.22	32.16	0.21	1.64	0.04	n.d.	n.d.	n.d.	n.d.	99.21	0.47	godlevskite
140	CS22_R13_1_12	42.41	0.17	0.67	0.03	1.19	0.03	n.d.	n.d.	n.d.	n.d.	44.27	0.24	

No.	Comment	Ni	\pm [wt%]	S	\pm [wt%]	Fe	\pm [wt%]	Cu	\pm [wt%]	Co	SD[wt%]	total	\pm [wt%]	mineral
141	CS22_R13_1_13	38.51	0.17	0.50	0.03	0.99	0.03	n.d.	n.d.	0.24	0.03	40.24	0.25	n.d.
142	CS22_R13_2_1	70.27	0.23	26.08	0.19	3.37	0.05	n.d.	n.d.	n.d.	n.d.	99.71	0.47	heazlewoodite
143	CS22_R13_2_2	67.20	0.22	32.24	0.21	1.42	0.04	n.d.	n.d.	n.d.	n.d.	100.86	0.46	godlevskite
144	CS22_R13_2_3	65.07	0.22	32.25	0.21	1.60	0.04	n.d.	n.d.	n.d.	n.d.	98.91	0.47	millerite
145	CS22_R13_2_4	70.16	0.22	2.93	0.06	23.97	0.12	n.d.	n.d.	1.25	0.04	98.30	0.46	awaruite
146	CS22_R13_2_5	41.16	0.17	0.77	0.03	0.98	0.03	n.d.	n.d.	n.d.	n.d.	42.90	0.23	n.d.
147	CS22_R13_2_6	63.06	0.21	33.92	0.21	1.68	0.04	n.d.	n.d.	n.d.	n.d.	98.66	0.47	millerite
148	CS22_R13_2_7	71.06	0.23	27.30	0.19	1.66	0.04	n.d.	n.d.	n.d.	n.d.	100.03	0.46	heazlewoodite
149	CS22_R13_2_8	65.31	0.22	33.83	0.21	1.55	0.04	n.d.	n.d.	n.d.	n.d.	100.69	0.47	millerite
150	CS22_R13_2_9	64.47	0.22	33.43	0.21	1.35	0.04	n.d.	n.d.	n.d.	n.d.	99.25	0.47	millerite
151	CS22_R13_2_10	64.13	0.22	31.31	0.20	1.35	0.04	n.d.	n.d.	n.d.	n.d.	96.79	0.46	(godlevskite)
152	CS22_R13_2_11	63.62	0.22	34.05	0.21	1.83	0.04	n.d.	n.d.	n.d.	n.d.	99.50	0.47	millerite

Appendix table 1. n.d.: not determined